Project acronym and title:
SECURe – Subsurface Evaluation of Carbon capture and storage and Unconventional risks

D5.5 REPORT ON THE SMALL-SCALE PROCESSES OCCURRING DURING ENGINEERED PRECIPITATION AND MODELS TO ASSIST IN THE UPSCALING

Authors and affiliation:
Chris Rochelle[1], Tom Liddy[1], Alicja Lacinska[1], Yukun Ji[2], Nicolaine Agofack[3], Pierre Cerasi[3]

[1]British Geological Survey, Environmental Science Centre, Nicker Hill, Keyworth, Nottingham, NG12 5GG, UK

[2]University of Nottingham, School of Chemistry, Geochemistry Group, Nottingham, NG7 2RD, UK

[3]SINTEF Industry, Department of Petroleum, S. P. Andersens vei 15B, 7031 Trondheim, Norway

Email of lead author:
pierre.cerasi@sintef.no

D5.5
Revision:1 (draft for definitive)

Project funded by the European Commission within the Horizon 2020 Programme		
Dissemination Level		
PU	*Public*	*X*
~~***CO***~~	~~*Confidential, only for members of the consortium (incl. the Commission Services)*~~	
~~***CL***~~	~~*Classified, as referred to in Commission decision 2001/844/EC*~~	

Deliverable number:	**5.5**
Deliverable name:	**REPORT ON THE SMALL-SCALE PROCESSES OCCURRING DURING ENGINEERED PRECIPITATION AND MODELS TO ASSIST IN THE UPSCALING**
Work package:	**WP5 Impact Mitigation and Remediation**
Lead WP/deliverable beneficiary:	SINTEF Industry

Status of deliverable		
	By	**Date**
Submitted (Author(s))	**N**N1, NN2, Nicolaine Agofack	**30.11.2020**
Verified (WP leader)	Pierre Cerasi	30.11.20
Approved (EB member)	Jonathan Pearce	30.11.20
Approved (Coordinator)	E HOUGH	30.11.20

Author(s)		
Name	**Organisation**	**E-mail**
Chris Rochelle	**B**GS	caro@bgs.ac.uk
Tom Liddy	**BGS**	tlid@bgs.ac.uk
Alicja Lacinska	**BGS**	alci@bgs.ac.uk
Yukun Ji	**U**NOTT	yukun.ji1@nottingham.ac.uk
Nicolaine Agofack	**SINTEF**	Nicolaine.agofack@sintef.no
Pierre Cerasi	**SINTEF**	Pierre.cerasi@sintef.no

Public introduction

The Subsurface Evaluation of CCS and Unconventional Risks (SECURe) project is gathering unbiased, impartial scientific evidence for risk mitigation and monitoring for environmental protection to underpin subsurface geoenergy development. The main outputs of SECURe comprise recommendations for best practice for unconventional hydrocarbon production and geological CO_2 storage. The project is funded from June 2018–May 2021.

The project is developing monitoring and mitigation strategies for the full geoenergy project lifecycle; by assessing plausible hazards and monitoring associated environmental risks. This is achieved through a program of experimental research and advanced technology development that includes demonstration at commercial and research facilities to formulate best practice. We will meet stakeholder needs; from the design of monitoring and mitigation strategies relevant to operators and regulators, to developing communication strategies to provide a greater level of understanding of the potential impacts.

The SECURe partnership comprises major research and commercial organisations from countries that host shale gas and CCS industries at different stages of operation (from permitted to closed). We are forming a durable international partnership with non-European groups; providing international access to study sites, creating links between projects and increasing our collective capability through exchange of scientific staff.

Executive report summary

This report presents laboratory and numerical modelling work carried out in WP5 to develop new methodologies for remediation of leakage paths susceptible to occur in and around CO2 injection wells. In the laboratory, work has been carried out on novel fluids, designed to precipitate when interacting with leaking CO2. One effort looks at precipitation of calcium carbonate inside fractures present in the well's cement sheath, when encountering the escaping CO2 stream (BGS). Promising first results are described for a calcium rich fluid. A second approach is described in this report, whereby magnesite is engineered to be more stable, as this precipitate could be a good candidate for acidic CO2 leakage conditions (UNOTT). One promising route is the addition of nanoparticles.

On the modelling front, a fracturing tool coupled to a fluid flow simulator is used to back-analyse the ECCSEL mini-wellbore simulator near-wellbore fracturing experiments described in detail in report D5.4 (SINTEF). By calibrating the tool to be able to qualitatively reproduce the same fracture patterns as observed in the laboratory for given stress conditions, one is able to alter the well structure dimensions and upscale the system to field conditions. Thus it is hoped that the tool will be useful to predict different fracturing scenarios for real well systems and also for the design of repeat test campaigns with other remediation fluids. The fracture patterns can then be exported to flow simulators to study permeability and thus plugging efficiency required from remediation fluids.

Contents

FIGURES

TABLES

1 Introduction

1.1 THE AIM OF THIS WORK

The work presented here was performed as part of the SECURe Work Package (WP) 5, specifically addressing the design of remediation chemistries. The intent was to design novel fluids that would lead to mineral precipitation or polymerisation reaction in contact with activating fluids, such as leaking CO_2. The intention was to obtain better performing remediation fluids than currently available, easy to deploy by injecting directly in damaged areas through a well, either itself connected to the leaking pathway or as a way to spread the fluid at depth towards its target placement. The chemistries were developed and tested at bench-top scale, since this is the fastest way to experiment with composition, dosage and controlled testing of achievement of the desired effect. In parallel, an initial effort was made to back-analyse the laboratory experiments conducted with the ECCSEL Well Integrity Research Infrastructure, a CT transparent mini-wellbore simulator situated at SINTEF's Petroleum Department. This equipment has been described in detail in report D5.4 "Guidelines on ranking of sealant materials": it consists of a concentric assembly of a downscaled steel casing, cemented into a hollow cylinder rock plug inside a sleeved pressure vessel. The cell has separate fluid ports permitting pressure control of the fluid in the central borehole, pressure control of the cement slurry in the annulus while curing, pore pressure control in the surrounding rock, and finally external confining pressure application on a thin oil film outside of the containing rubber sleeve. The numerical model developed was calibrated to be able to recreate within reasonable agreement the observed radial fractures obtained under cyclic pressurisation of the steel casing against its cement sheath. These results now open the way for upscaling, both in terms of system dimensions (to equal field well sizes) and external boundary conditions, where the effect of the finite size of the confining pressure cell are relaxed.

1.2 REMEDIATION FLUIDS: BGS FLUID-MIXING DESCRIPTION

The concept underpinning the work is injection of alkaline, Ca-rich water into regions with unwanted migration of CO_2-rich fluids – in the case studied here, the engineered seal of a borehole. Reaction of the dissolved Ca with CO_2 (free phase or dissolved) will increase the degree of saturation with respect to carbonate minerals, in particular calcite (though other polymorphs such as aragonite and vaterite are possible). Precipitation of carbonates will reduce the size of flow paths, reduce permeability, and so reduce, and ideally stop, unwanted CO_2 flow. The primary aim of this work is to demonstrate that this reaction has the potential to lower permeability, with a secondary aim of quantifying its impact on permeability.

$$Ca^{2+} + CO_2 + 2\,OH^- \Rightarrow CaCO_3 + H_2O$$

For this work, we chose an aqueous phase over cement grout because of its lower viscosity and better ability to penetrate smaller flow paths. Potential regions under consideration in this study include: 1) the cement seal of a borehole (e.g. a poor ‘cement job’ can leave incomplete sealing, or a borehole being reused after hydrocarbon production may have developed fractures in the cement or debonding as a consequence of pressure/temperature cycling during production operations), 2) potentially the drilling-induced damage zone around a borehole.

A key part of the concept underpinning this work is that the migrating CO_2 forms half of the reaction. Consequences of this are that: 1) less material will need to be injected to effect sealing (which may offer financial and logistical benefits), 2) reaction-induced precipitation will only happen where the CO_2 is present, and thus, the approach specifically targets pathways of CO_2 flow. As carbonate minerals are stable over geologic timescales they have the potential to act as effective, long-term seals.

In initial tests, we considered the case of migration of a CO_2-saturated saline fluid. This was prioritised for initial study as a slightly acidic aqueous fluid can dissolve borehole cement, and hence potentially has the ability to erode an already imperfect cement seal, further increasing permeability in a positive feedback loop. In Sections 2 and 3, we detail our measurements of flow changes, initial mineralogical observations, and preliminary conclusions.

A further test considered reaction with free CO_2. Though cement minerals do not dissolve in free CO_2, and hence the reaction will not erode cement through dissolution, it will cause carbonation of cement – likely causing changes in solids volume, and possibly changing cement bonding properties. In Sections 2 and 3, we

just present initial observations of flow changes, as mineralogical studies are ongoing at the time of writing this report.

Observations and interpretations from subsequent tests will be reported in later deliverables.

1.3 REMEDIATION CHEMISTY WORK AT UNOTT

Carbon sequestration through underground storage of captured CO_2 into reservoirs in deep geologic formations is an efficient way to control global warming, whereas the CO_2 leakage pathways have led to a considerable concern. CO_2 leakage and/or brine coming from CO_2 geological storage sites can pose a risk for overlying fresh groundwater resource, resulting in a low pH, variation in redox potential, change of microbial metabolism, and potential contaminant mobilisation. Moreover, high CO_2 concentrations and long-term exposure in air could cause adverse consequences (e.g. narcosis, headache, and dizziness). Specific procedures for mitigating and remediating CO_2 leakage should be proposed to minimise CO_2 leakage induced potential environmental and health impacts.

Given the conventional grouts cannot easily penetrate into narrow pores and fractures in rocks, aqueous solutions with low viscosity that can pass through small pores are more promising. Precipitants produced through the chemical reaction between the solution and leaking CO_2 can fill up and plug pores or open fractures of a high permeable zone (e.g. calcium hydroxide could generate pore blocking-carbonate mineral in contact with CO_2). However, the plugging induced CO_2 accumulation at the outlet could result in a decrease in pore water pH, and thus drives the gradual dissolution of $CaCO_3$. Hence, an optimum technology could not only lead to a large degree of permeability reduction but also remain stable under a CO_2 leakage scenario (acidic environment).

The formation of acid-resistant precipitates that can effectively block CO_2 leakage mitigate risks involved with underground CO2 storage and offer solutions for remediation. Magnesite ($MgCO_3$) can be treated as a more acid-resistant mineral compared to those of calcite and dolomite in acidic scenario. Unfortunately, multiple metastable hydrated magnesium carbonate (e.g. $MgCO_3 \cdot 3H_2O$, $MgCO_3 \cdot 5H_2O$, and $(MgCO_3)_4 \cdot Mg(OH)_2 \cdot 4H_2O$) and hydroxide phases ($Mg(OH)_2$) form in the conversion of CO_2 to magnesite. Generally, the hydrated magnesium carbonates are more soluble and less effective for long term plugging of pore space. Here, we conducted batch reactor experiments to investigate the accelerated conversion of anhydrous magnesite (acid-resistant precipitate) by interaction of $MgCl_2$ with Na_2CO_3 under various scenarios (acidity, alkalinity, electrolytes, nanoparticles). This research improves our understanding of the chemical pathways behind the catalysis of anhydrous magnesite (metastable magnesium carbonate-to-anhydrous magnesite replacement) under different conditions, and may provide an environmental solution for effective remediation of CO_2 leakage.

1.4 NEAR-WELL FRACTURING MODELLING (SINTEF)

Wells play an important role in subsurface activities such as oil/gas exploitation, CO_2 and hydrogen storage. During these activities, wells are submitted to various mechanical and thermal loading with can lead to the creation of fractures in the near-well region (cement sheath and rock formation), and thus be potential leakage paths. Analytical and numerical understanding of the stress distribution that may lead to fractures around the near-well is therefore crucial. Depending on the casing, cement sheath, formation properties, and the in-situ stresses, the analytical model predicts the induced pressure which can lead to fracture creation, while a numerical tool is used to model the propagation of these fractures.

1.4.1. **Analytical description**

Let us consider the structure shown in Figure 1. A hole goes through three different formations. The steel hollow cylinder (called ***casing***) and a cement sheath that fills the annulus space between the casing and the formation rock is usual in well construction. But it can happen in some depths that the formation is directly in contact with the casing or even that the hole is totally opened, especially in the reservoir. The in-situ stresses are usually anisotropic. σ_1 and σ_2 are perpendicular to the hole axis. The casing pressure is denoted P_i, and will be sometimes referred to as hole pressure or inner pressure.

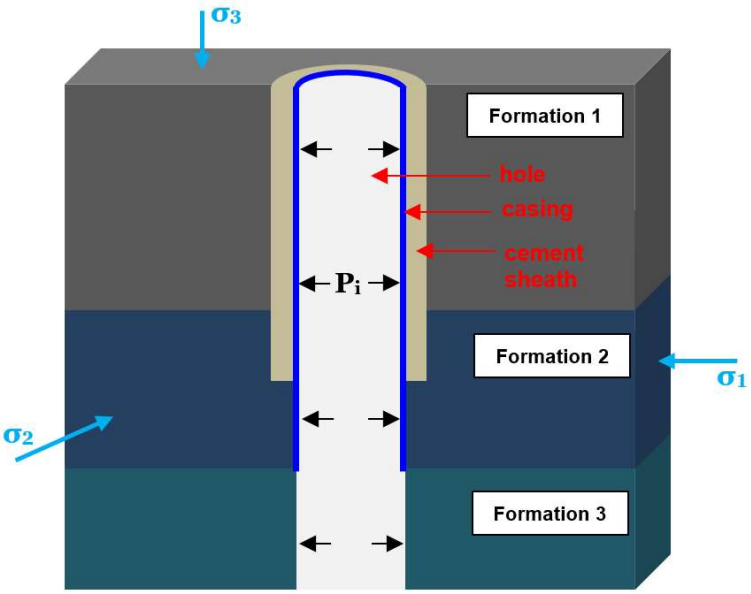

Figure 1. Well architecture, usually composed of hole, casing and cement sheath

Jaeger et al., 2007, showed that the stresses and displacements can be derived from two complex potentials. If $\phi(z)$ and $\psi(z)$ are those complex potentials, the displacements and stresses in cartesian coordinates are given by the following expressions:

$$2G(u+iv) = \kappa\phi(z) - z\overline{\phi'(z)} - \overline{\psi(z)} \quad (1)$$

$$\tau_{xx} + \tau_{yy} = 2\left[\phi'(z) + \overline{\phi'(z)}\right] \quad (2)$$

$$\tau_{yy} - \tau_{xx} + 2i\tau_{xy} = 2\left[\bar{z}\phi''(z) + \psi'(z)\right] \quad (3)$$

where G is the shear modulus of the material, u and v the displacements in the x- and y-directions, respectively. $\overline{\chi} = \chi_1 - i\chi_2$ represents the conjugate of the complex function $\chi = \chi_1 + i\chi_2$; χ' and χ'' first and second derivative of χ, $z = x + iy$ is a complex variable, with i the complex number ($i^2 = -1$). κ is a function of Poisson's ratio ν: $\kappa = 3 - 4\nu$ for plane strain ($\varepsilon_1 \neq 0,\ \varepsilon_2 \neq 0,\ \varepsilon_3 = 0$) and $\kappa = (3-\nu)/(1+\nu)$ for plane stress ($\sigma_1 \neq 0,\ \sigma_2 \neq 0,\ \sigma_3 = 0$). In polar coordinates, the stresses and displacements are derived from equations (1)-(3) as follows:

$$u_r + iu_\theta = (u+iv)e^{-i\theta} \quad (4)$$

$$\tau_{rr} + \tau_{\theta\theta} = \tau_{xx} + \tau_{yy} \quad (5)$$

$$\tau_{\theta\theta} - \tau_{rr} + 2i\tau_{r\theta} = (\tau_{yy} - \tau_{xx} + 2i\tau_{xy})e^{2i\theta} \quad (6)$$

The traction in the material is expressed by:

$$2(N - iT) = \tau_{yy} + \tau_{xx} - (\tau_{yy} - \tau_{xx} + 2i\tau_{xy})e^{2i\theta} \quad (7)$$

where N and T are its normal and shear components, respectively. $e^{i\theta} = \cos\theta + i\sin\theta$. In these polar coordinates, the complex variable is given by $z = re^{i\theta}$. The strains are defined by:

$$\varepsilon_{rr} = \frac{\partial u_r}{\partial r};\quad \varepsilon_{\theta\theta} = \frac{1}{r}\frac{\partial u_\theta}{\partial \theta} + \frac{u_r}{r};\quad \varepsilon_{r\theta} = \frac{1}{2}\left(\frac{\partial u_\theta}{\partial r} + \frac{1}{r}\frac{\partial u_r}{\partial \theta} - \frac{u_\theta}{r}\right) \quad (8)$$

where u_r and u_θ are radial and tangential displacement, ε_{rr}, $\varepsilon_{\theta\theta}$ and $\varepsilon_{r\theta}$ the radial, tangential and shear strain, respectively, and θ the Lode angle.

Let us consider the simple case of a hollow cylinder, as presented in Figure 2 with inner and outer radii, a and b, inner and outer pressure, P_i and P_o, respectively. According to Jaeger et al. (2007), the complex potentials for this configuration are given by:

$$\phi(z) = cz; \qquad \psi(z) = \frac{d}{z} \tag{9}$$

where c and d are constants of real numbers. The boundary conditions on the inner and outer surfaces are fulfilled by continuity of traction at inner and outer boundary, which is reduced to: $\tau_{rr}(r=a) = P_i$ and $\tau_{rr}(r=b) = P_o$. Combining this with (1) - (9), c and d are then given by: $c = \frac{1}{2}\frac{b^2P_o - a^2P_i}{b^2 - a^2}$ and $d = \frac{a^2b^2(P_i - P_o)}{b^2 - a^2}$.

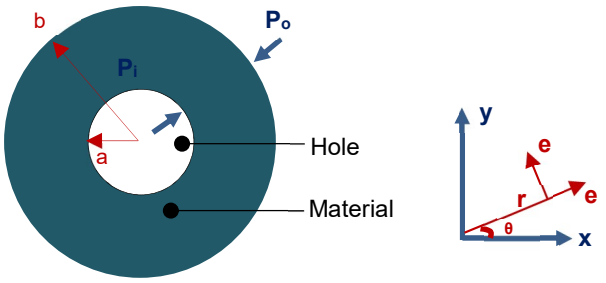

Figure 2. Hollow cylinder

The displacements, strains and stresses are then given in relations (10)-(14) as functions of the radii a and b as well as the applied pressures P_i and P_o.

$$u_r = \frac{(\kappa-1)}{4G}\frac{\left(b^2P_o - a^2P_i\right)}{b^2 - a^2}r - \frac{1}{2G}\frac{a^2b^2\left(P_i - P_o\right)}{\left(b^2 - a^2\right)r} \tag{10}$$

$$\varepsilon_{rr} = \frac{(\kappa-1)}{4G}\frac{\left(b^2P_o - a^2P_i\right)}{b^2 - a^2} + \frac{1}{2G}\frac{a^2b^2\left(P_i - P_o\right)}{\left(b^2 - a^2\right)r^2} \tag{11}$$

$$\varepsilon_{\theta\theta} = \frac{(\kappa-1)}{4G}\frac{\left(b^2P_o - a^2P_i\right)}{b^2 - a^2} - \frac{1}{2G}\frac{a^2b^2\left(P_i - P_o\right)}{\left(b^2 - a^2\right)r^2} \tag{12}$$

$$\tau_{rr} = \frac{b^2P_o - a^2P_i}{b^2 - a^2} + \frac{a^2b^2\left(P_i - P_o\right)}{\left(b^2 - a^2\right)r^2} \tag{13}$$

$$\tau_{\theta\theta} = \frac{b^2P_o - a^2P_i}{b^2 - a^2} - \frac{a^2b^2\left(P_i - P_o\right)}{\left(b^2 - a^2\right)r^2} \tag{14}$$

It is worth noting that these expressions are independent of the Lode angle θ. If for example the properties of Table 1 are used, at a fixed applied outer pressure of 15 MPa, the graphs of Figure 3 give the varying strains and stresses with the inner pressure. The tangential stress in the material becomes negative near the inner radius for higher values of inner pressure. When this negative value becomes higher than that the tensile strength of the rock, this will lead to tensile failure in the material. From results of $\tau_{\theta\theta}$ displayed in Figure 3, it is clear that the material will fail from the inner surface and the fracture will propagate to the outer surface. The sizes in the following Tables are chosen based on an experiment setup, that will be presented in a next section.

Table 1. Rock properties

Material	Formation
Size	a = 18.5 mm
	b = 45.0 mm
E (GPa)	12.0
v [-]	0.25

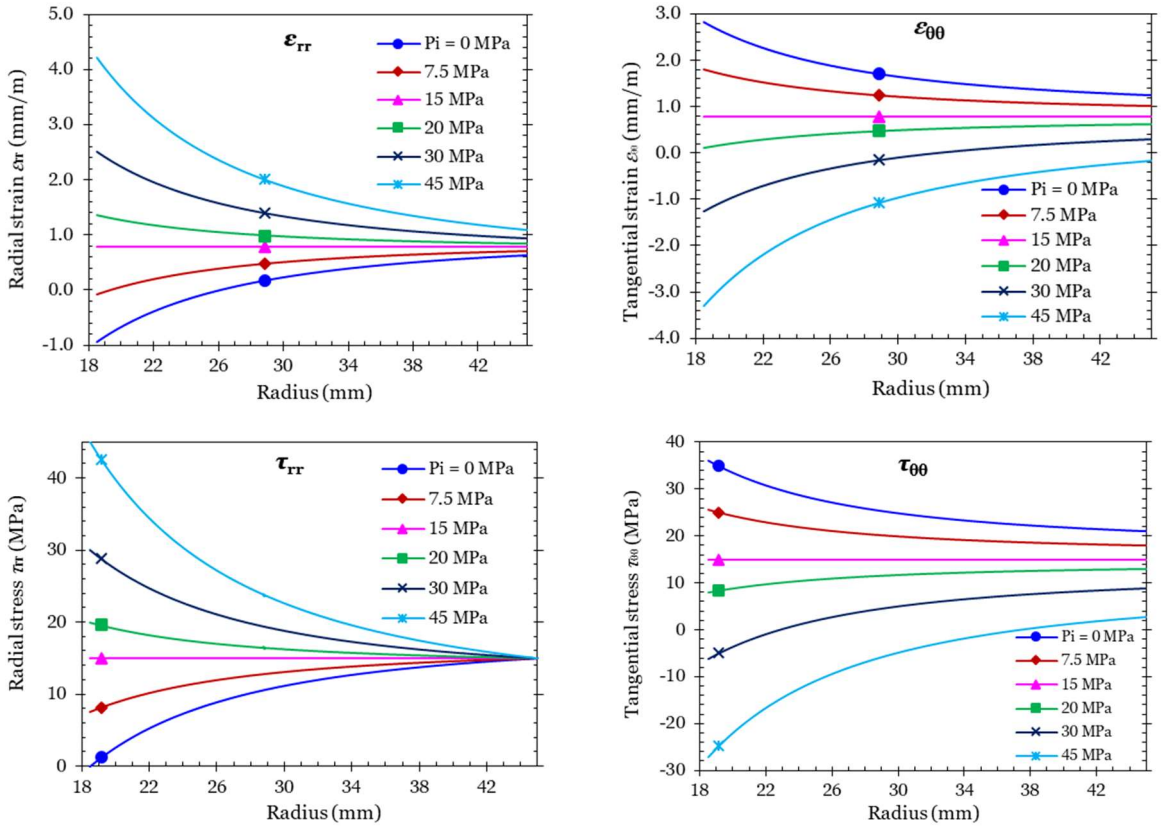

Figure 3. Strains and stresses as a function of radius for different hole pressure P_i and at a constant outer pressure (P_o = 15 MPa)

The problem of Figure 2 can be extended to the field with far-field anisotropic applied stresses, σ_1^∞ and σ_2^∞, as presented in Figure 4. The actions of P_i, σ_1^∞ and σ_2^∞ on the displacement field and stress field around the hole are evaluated using the superposition principle. When there is no far-field stresses ($\sigma_1^\infty = \sigma_2^\infty = 0$), the effect of P_i on strains, stresses and displacements are obtained from relations (10)-(14) extending b to infinite and P_o to zero. For the only effect of σ_1^∞, the hole is assumed free from pressure ($P_i = 0$) and the principal stress in the y-direction is also assumed zero ($\sigma_2^\infty = 0$). The following forms are proposed for complex potentials:

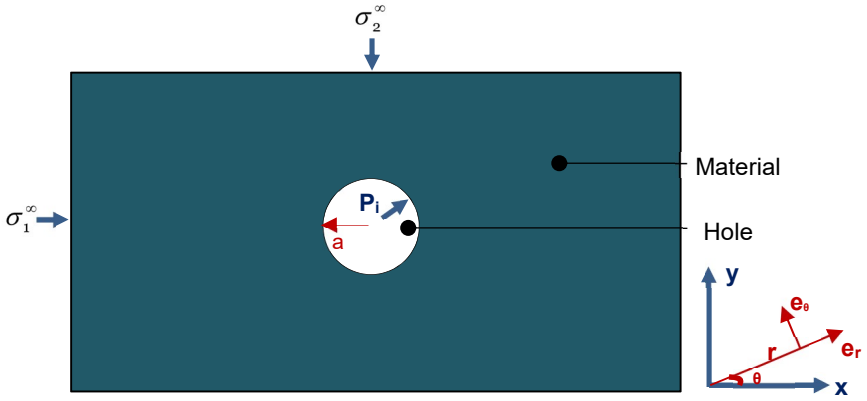

Figure 4. Hole in rock formation with far-field anisotropic principal stresses

$$\phi(z) = \frac{1}{4}\sigma_1^\infty\left(z + \frac{A}{z}\right); \qquad \psi(z) = -\frac{1}{2}\sigma_1^\infty\left(z + \frac{B}{z} + \frac{C}{z^3}\right) \tag{15}$$

where Z is the complex variable, A, B and C constants which are assumed real numbers. Combining this with (1)-(9), the constants A, B and C are then given by: $A=2a^2$; $B=a^2$; $C=-a^4$. The stresses and displacement are then given by:

$$u_r=\frac{\sigma_1^\infty}{4G}\left[\frac{(\kappa-1)}{2}r+\frac{a^2}{r}+\left(r+\frac{(\kappa+1)a^2}{r}-\frac{a^4}{r^3}\right)\cos 2\theta\right] \tag{16}$$

$$u_\theta=-\frac{\sigma_1^\infty}{4G}\left(r+\frac{(\kappa-1)a^2}{r}-\frac{a^4}{r^3}\right)\sin 2\theta \tag{17}$$

$$\tau_{rr}=\frac{1}{2}\sigma_1^\infty\left[1-\frac{a^2}{r^2}+\left(1-\frac{4a^2}{r^2}+\frac{3a^4}{r^4}\right)\cos 2\theta\right] \tag{18}$$

$$\tau_{\theta\theta}=\frac{1}{2}\sigma_1^\infty\left[1+\frac{a^2}{r^2}-\left(1-\frac{3a^4}{r^4}\right)\cos 2\theta\right] \tag{19}$$

$$\tau_{r\theta}=-\frac{1}{2}\sigma_1^\infty\left(1+\frac{2a^2}{r^2}-\frac{3a^4}{r^4}\right)\sin 2\theta \tag{20}$$

The effects of σ_2^∞ on the displacements and stresses are similar to those of σ_1^∞. Since σ_2^∞ is oriented $\frac{\pi}{2}$ from σ_1^∞, the angle θ is then replaced by $\theta+\frac{\pi}{2}$. The combined effects of P_i, σ_1^∞ and σ_2^∞ are expressed in equations (21)-(25). Using equation (8), the strains can also be derived. The tangential displacement and the shear components of stress and strain are independent of the inner pressure.

$$u_r=\frac{\sigma_1^\infty+\sigma_2^\infty}{4G}\left[\frac{(\kappa-1)}{2}r+\frac{a^2}{r}\right]+\frac{\sigma_1^\infty-\sigma_2^\infty}{4G}\left[r+\frac{(\kappa+1)a^2}{r}-\frac{a^4}{r^3}\right]\cos 2\theta-\frac{P_\mathrm{i}}{2G}\frac{a^2}{r} \tag{21}$$

$$u_\theta=-\frac{\sigma_1^\infty-\sigma_2^\infty}{4G}\left[r+\frac{(\kappa-1)a^2}{r}-\frac{a^4}{r^3}\right]\sin 2\theta \tag{22}$$

$$\tau_{rr}=\frac{\sigma_1^\infty+\sigma_2^\infty}{2}\left(1-\frac{a^2}{r^2}\right)+\frac{\sigma_1^\infty-\sigma_2^\infty}{2}\left(1-\frac{4a^2}{r^2}+\frac{3a^4}{r^4}\right)\cos 2\theta+P_\mathrm{i}\frac{a^2}{r^2} \tag{23}$$

$$\tau_{\theta\theta}=\frac{\sigma_1^\infty+\sigma_2^\infty}{2}\left(1+\frac{a^2}{r^2}\right)-\frac{\sigma_1^\infty-\sigma_2^\infty}{2}\left(1-\frac{3a^4}{r^4}\right)\cos 2\theta-P_\mathrm{i}\frac{a^2}{r^2} \tag{24}$$

$$\tau_{r\theta}=-\frac{\sigma_1^\infty-\sigma_2^\infty}{2}\left(1+\frac{2a^2}{r^2}-\frac{3a^4}{r^4}\right)\sin 2\theta \tag{25}$$

Using the rock parameters presented in Table 1, and the far-field principal stresses $\sigma_1^\infty=\sigma_\mathrm{H}=10\ \mathrm{MPa}$ and $\sigma_2^\infty=\sigma_\mathrm{h}=8\ \mathrm{MPa}$ in the x- and y-directions, respectively. As shown in equations (21)-(25), the displacements, strains and stresses are functions of the Lode angle θ, of the radius and of inner pressure P_i. For an inner pressure of 7 MPa, the variation in displacements, strains and stresses are given at the borehole wall ($r = a$) and inside the rock ($r = 1.5\times a$). The radial stress τ_{rr} at the borehole wall is not affected by the Lode angle. The strain and stress distribution are given in Figure 6 for different inner pressure, along the x-axis ($\theta = 0°$). The radial and tangential stress converge to a single value at infinity.

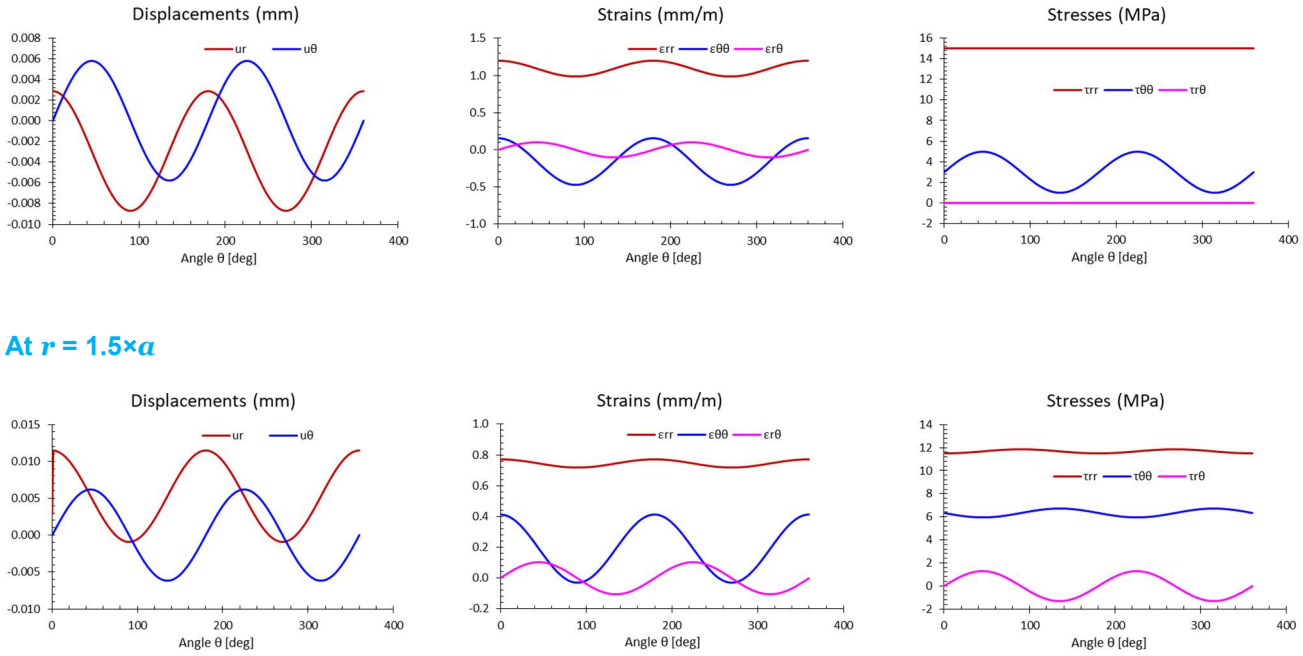

Figure 5. Displacements, strains, and stresses as a function of the Lode angle θ at the $r = a$ and at $r = 1.5 \times a$ for an inner pressure (P_i = 7 MPa)

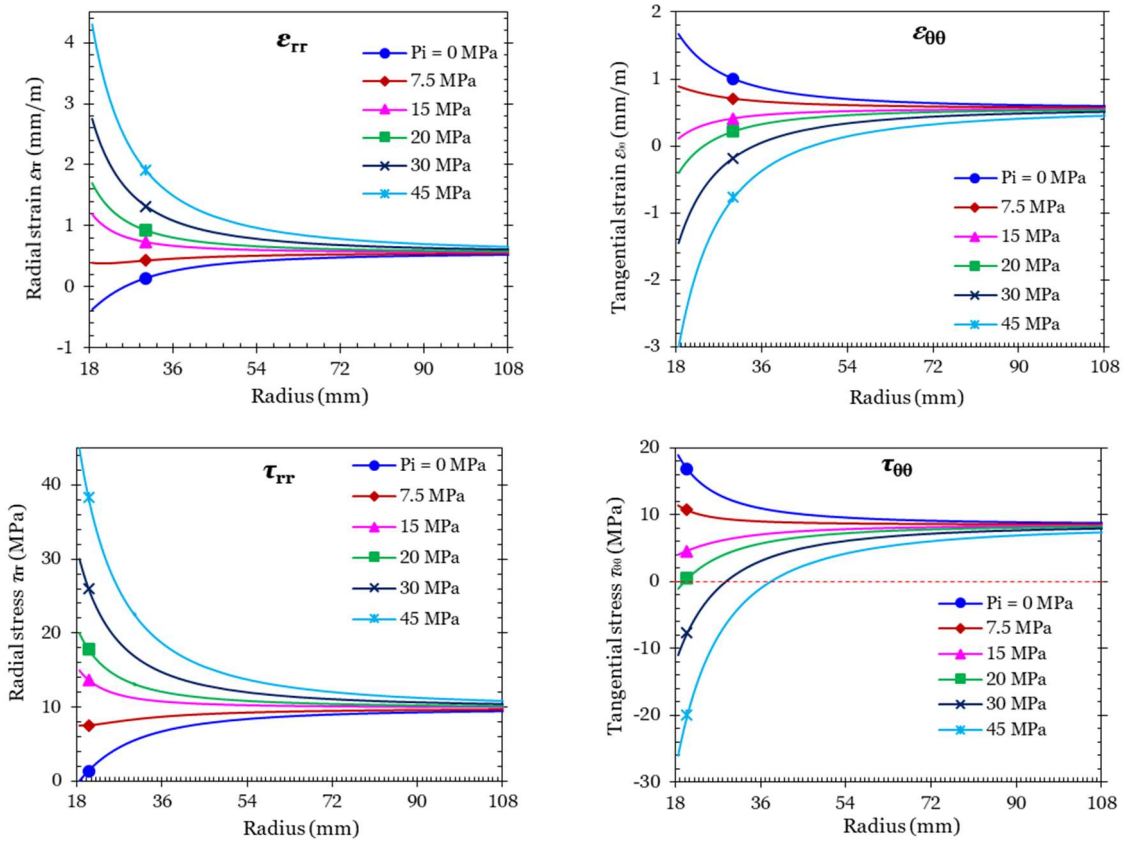

Figure 6. Strains and stresses distribution in the material at the Lode angle θ = 0°

Three concentric hollow cylinders are now considered. They are composed of a casing, cement, and rock (see Figure 1, on Formation 1's section). The casing has an inner radius a and outer radius a_1. The inner radius of the rock is a_2 and the outer radius b. The three materials are characterised by their shear modulus and Poisson ration (G_i, ν_i), with i =1,2,3 stand for casing, cement and rock, respectively. Continuity of displacement and radial stress is assumed at all interfaces (casing/cement and cement/rock). At the inner surface of the casing, the radial pressure is equal to P_i, while at the outer surface of the rock, it is P_o. The complex potentials, similar to those proposed in (9), are considered for each material of Figure 7 and give in (26).

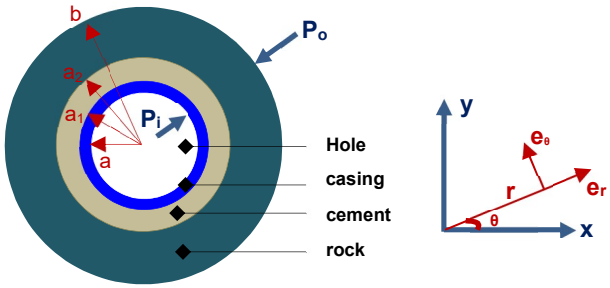

Figure 7. concentric hollow cylinders

$$\phi_i(z) = c_i z; \quad \psi_i(z) = \frac{d_i}{z} \tag{26}$$

where c_i and d_i are real constants (with i =1,2,3), ϕ_i, ψ_i the complex potentials in each material, and z the complex variable. In total there are six unknown constants; six equations are then needed to find those constants: two equations are from displacement continuity, two from traction continuity and two from the boundary conditions at the inner surface of the casing and at the outer surface of the rock.

Using equations (1), (4) and (26), the displacements in the different materials are given by:

$$u_r + iu_\theta = \frac{1}{2G_1}\left[(\kappa_1 - 1)c_1 r - \frac{d_1}{r}\right]; \quad a \le r \le a_1 \tag{27}$$

$$u_r + iu_\theta = \frac{1}{2G_2}\left[(\kappa_2 - 1)c_2 r - \frac{d_2}{r}\right]; \quad a_1 \le r \le a_2 \tag{28}$$

$$u_r + iu_\theta = \frac{1}{2G_3}\left[(\kappa_3 - 1)c_3 r - \frac{d_3}{r}\right]; \quad a_2 \le r \le b \tag{29}$$

There is continuity of displacement at a_1 and a_2.

$$u_r + iu_\theta\big|_{r=a_1} = \frac{1}{2G_1}\left[(\kappa_1 - 1)c_1 a_1 - \frac{d_1}{a_1}\right] = \frac{1}{2G_2}\left[(\kappa_2 - 1)c_2 a_1 - \frac{d_2}{a_1}\right] \tag{30}$$

$$u_r + iu_\theta\big|_{r=a_2} = \frac{1}{2G_2}\left[(\kappa_2 - 1)c_2 a_2 - \frac{d_2}{a_2}\right] = \frac{1}{2G_3}\left[(\kappa_3 - 1)c_3 a_2 - \frac{d_3}{a_2}\right] \tag{31}$$

From equations (30) and (31), the following relations are obtained:

$$(\kappa_1 - 1)a_1^2 c_1 - d_1 = \beta_1(\kappa_2 - 1)a_1^2 c_2 - \beta_1 d_2; \quad \beta_1 = G_1 / G_2 \tag{32}$$

$$(\kappa_2 - 1)a_2^2 c_2 - d_2 = \beta_2(\kappa_3 - 1)a_2^2 c_3 - \beta_2 d_3; \quad \beta_2 = G_2 / G_3 \tag{33}$$

Using equations (2)-(3), (5)-(7)and (26), the tractions in the materials are given by:

$$N - iT = 2c_1 + \frac{d_1}{r^2}; \quad a \le r \le a_1 \tag{34}$$

$$N - iT = 2c_2 + \frac{d_2}{r^2}; \quad a_1 \le r \le a_2 \tag{35}$$

$$N - iT = 2c_3 + \frac{d_3}{r^2}; \quad a_2 \le r \le b \tag{36}$$

Following the assumption of traction continuity at interfaces ($r = a_1$ and $r = a_2$), this leads to:

$$2a_1^2 c_1 + d_1 = 2a_1^2 c_2 + d_2 \tag{37}$$

$$2a_2^2 c_2 + d_2 = 2a_2^2 c_3 + d_3 \tag{38}$$

Using the boundary conditions ($\tau_{rr}(a) = P_i$ and $\tau_{rr}(b) = P_o$), the following two relations are also obtained:

$$a^2 P_i = 2a^2 c_1 + d_1 \tag{39}$$

$$b^2 P_o = 2b^2 c_3 + d_3 \tag{40}$$

The relations (32), (33), and (37)-(40) are then used to evaluate the six unknown constants c_i and d_i. The following solution is found:

$$c_1 = \frac{\alpha_3}{2\alpha_1} P_o - \frac{\alpha_2}{2\alpha_1} P_i \tag{41}$$

where α_i are dimensionless and are given by:

$$\alpha_1 = \frac{a_1^2 - a^2}{b^2} + \frac{\chi_2 \delta_1}{\beta_1 \chi_1}; \quad \alpha_2 = \left(1 - \frac{2\chi_2}{\beta_1 \chi_1}\right)\frac{a^2}{b^2}; \quad \alpha_3 = \left(1 - \frac{2\chi_2}{\chi_1}\right)\chi_3 \tag{42}$$

χ_i and δ_i are dimensionless parameters and given by:

$$\chi_1 = \delta_2 + 2\frac{b^2 - a_2^2}{b^2}\frac{a_2^2}{b^2}\frac{(\kappa_2 + 1)}{\delta_3} \tag{43}$$

$$\chi_2 = \frac{a_2^2 - a_1^2}{b^2} + \frac{b^2 - a_2^2}{b^2}\frac{a_2^2}{b^2}\frac{(\kappa_2 + 1)}{\delta_3} \tag{44}$$

$$\chi_3 = 1 + 2\frac{b^2 - a_2^2}{b^2}\frac{(1 - \beta_2)}{\delta_3} \tag{45}$$

and

$$\delta_1 = \frac{(\kappa_1 + 1)a_1^2 - 2(a_1^2 - a^2)}{b^2} \tag{46}$$

$$\delta_2 = \frac{(\kappa_2 + 1)a_1^2 + 2(a_2^2 - a_1^2)}{b^2} \tag{47}$$

$$\delta_3 = \beta_2(\kappa_3 + 1)\frac{a_2^2}{b^2} - 2(1 - \beta_2)\left(1 - \frac{a_2^2}{b^2}\right) \tag{48}$$

where β_i are as defined in (32) and (33), and κ_i are functions of Poisson's ratio in the different materials. From equation (41), the others constants can be determined successfully and are given by (49)-(53).

$$c_2 = \frac{\delta_1}{\beta_1 \chi_1} c_1 - \frac{a^2}{\beta_1 \chi_1 b^2} P_i + \frac{\chi_3}{\chi_1} P_o \tag{49}$$

$$c_3 = \frac{a_2^2}{b^2}\frac{(\kappa_2 + 1)}{\delta_3} c_2 - \frac{(1 - \beta_2)}{\delta_3} P_o \tag{50}$$

$$d_2 = b^2 P_o - 2a_2^2 c_2 - 2(b^2 - a_2^2)c_3 \tag{51}$$

$$d_1 = a^2\left(P_i - 2c_1\right) \tag{52}$$

$$d_3 = b^2\left(P_o - 2c_3\right) \tag{53}$$

Using the parameters defined in Table 2, some computations of stress and strain distributions are presented in Figure 8 for different casing pressure, with a fixed outer pressure of 15 MPa. The tangential strain and radial stress are continuous through the interfaces, while the radial strain and tangential stress are highly discontinuous. Increasing the casing pressure, the radial stress and radial strain increase, while the tangential stress and strain decrease. Particularly, for the casing pressure up to 20 MPa, the tangential stress is compressive (positive). When the casing pressure is increased to 30 MPa, the tangential stress becomes tensile (negative) and can lead to tensile failure if the absolute value of that tensile stress exceeds the tensile strength of the material.

Table 2. Materials properties

Material	Casing	Cement	Formation
Size	a = 18.5 mm	a_1 = 20 mm	a_2 = 26 mm
	a_1 = 20 mm	a_2 = 26 mm	b = 45 mm
E (GPa)	200	7.0	12.0
v [-]	0.3	0.15	0.25

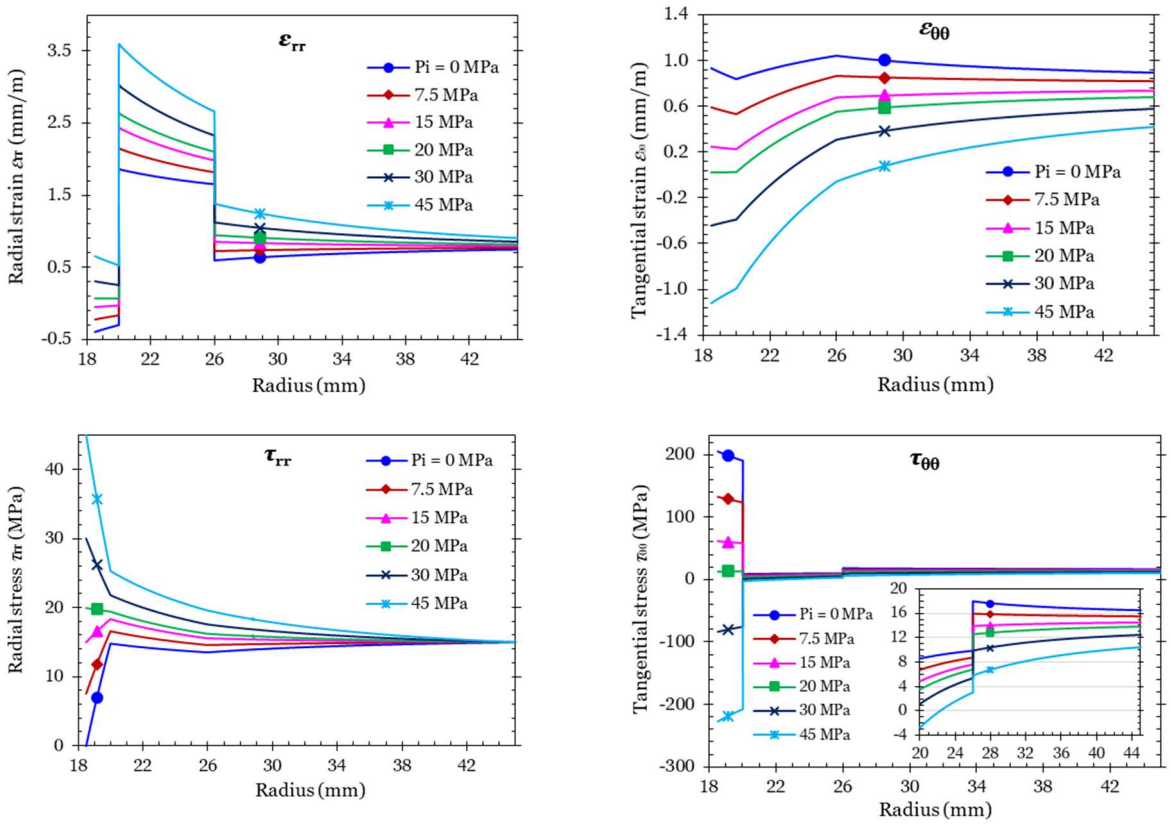

Figure 8. Strains and stresses as a function of casing pressure for constant pressure applied to the formation: P_o = 15 MPa

In the case where the casing pressure equals the outer applied stress ($P_i = P_o$ = 15 MPa), the stress distribution for different rock properties is given in Figure 9. In the uniform case (similar to Figure 2), all the materials have the same properties, the stresses are then constants and equal to 15 MPa. When having different materials

(as in Figure 7, and Table 3), the stresses are not anymore constants even if the inner and outer pressures are equal.

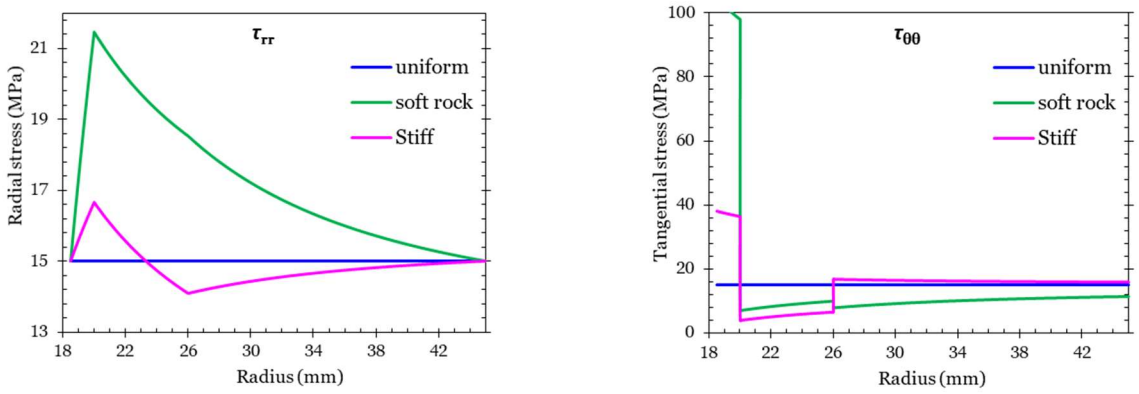

Figure 9. Radial and tangential stresses for different materials when $P_i = P_o = 15$ MPa

Table 3. Soft and stiff rock

	Material	Casing	Cement	Formation
	Thickness: a = 18.5 mm; b = 45 mm	1.5 mm	6 mm	19 mm
SOFT	*E* (GPa)	200	8.0	**2.0**
	v [-]	0.3	0.15	**0.25**
STIFF	*E* (GPa)	200	8.0	**30**
	v [-]	0.3	0.15	**0.15**

1.4.2. **Numerical description**

The analytical solution as presented in the precedent section gives the stress distribution in the materials around the well. It can help predicting the potential regions that will fail in the material. However, it cannot be capable of simulating the fracture propagation. The modified discrete element method (MDEM) code, developed at SINTEF, is used to simulate fracture propagation in the near-well. Written in MATLAB, C/C++, this code was first developed by Alassi (2008, 2012) for failure in the context of reservoir geomechanics. Its use has been extended to reservoir pressurization, hydraulic fracturing, fault reactivation (Rongved and Cerasi, 2019) as well as casing pressurization (Gheibi et al., 2019). MDEM is a hybrid code, which can capture both continuum (in elastic regime) and discontinuum (when an element fails) behaviour of material. The elements in the code, as presented in Figure 10, can only be triangles in 2D or tetrahedra in 3D, and the boundary conditions are given in cartesian coordinates. The code is coupled with the open source MATLAB Reservoir Simulation Toolbox (MRST) code for fluid flow. This coupling makes it possible to simulate fracture propagation and fluid flow into the fracture.

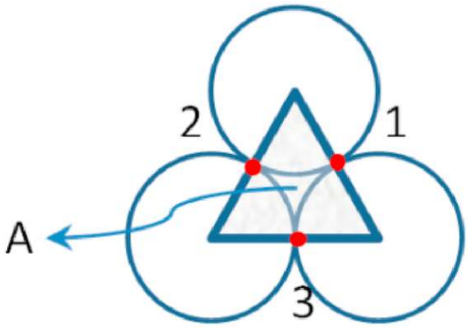

Figure 10. An element in MDEM. The red dots show the contacts and their allocated ID (Alassi, 2008). A triangle element (continuum) made of the centres of three particles that are connected by springs. A force is transmitted when a relative displacement occurs between the particles.

2 Experimental

2.1 DETAILED BGS EXPERIMENTAL WORK SO FAR

2.1.1 Starting materials

Cement:

The cement was prepared and cured as described in deliverable report D5.4, and delivered to the BGS laboratories sealed inside 1 litre plastic bottles. These were left tightly closed to prevent reaction with atmospheric CO_2, and only cut open and core plugs taken when required for the experiments. Four core plugs could be cut from each bottle of cured cement. Once taken, the 3.5 cm diameter core plugs were trimmed to a length of 12.5 cm, and then sliced longitudinally.

Aqueous solutions:

A 0.55 M NaCl solution (approximately seawater salinity) was used to displace any air and condition the cement core at the start of each experiment.

During the 'reaction' phase of the experiments, the aqueous phases consisted of:

1) 0.55 M NaCl saturated with CO_2 at the pressure and temperature of the experiment.
2) 0.55 M NaCl saturated with $Ca(OH)_2$ at room temperature (20°C). Any residual solid $Ca(OH)_2$ was removed prior to the $Ca(OH)_2$-saturated solution being heated to 50°C

We recognise that these are simplified compositions, but this maximises broader applicability. The use of just Ca-hydroxide also maximises Ca concentration, and hence increases our ability to track flow and mineralogical changes in these (relatively short duration) lab experiments. Note that $Ca(OH)_2$ has retrograde solubility, and some of it will precipitate in the conditioning vessel when heated to 50°C. This ensured that the solution was fully-saturated at 50 °C, and precipitation did not impair the functioning of the equipment.

Increasing the pH of the Ca-rich solution will favour carbonate mineral precipitation, and strong alkalis (such as NaOH or KOH) could be used for this. However, these alkalis can also reduce $Ca(OH)_2$ solubility, thus lower dissolved Ca concentration, and hence reduce amounts of potential carbonate precipitate formed. We plan to consider mixed hydroxide fluids in subsequent experiments (to be reported in a later WP5 deliverable).

CO_2:

Pure CO_2 was used in these experiments, delivered to the BGS from Air Products. In the cylinders, it was in liquid form, with the head space in the cylinders pressurised to approximately 2000 psi by helium gas. The CO_2 was transferred to pumps which were used to control pressure in the experiments. In the experiments both free-phase CO_2 was used, as well as CO_2 that was first dissolved in saline water under well-controlled pressure/temperature conditions.

2.1.2 Experimental arrangement

The cement first had its sliced surfaces roughened with emery paper, which also served to remove any high spots remaining from cutting. Slightly rough surfaces were beneficial, as they: a) were closer to real-world situations (e.g. likely providing energetically-favourable nucleation points for new precipitates), b) better enabled flow, as smooth surfaces can clamp together under high confining pressures and prevent flow. PEEK endcaps were added to each end of the core and the assembly sheathed in black heat-shrink PVC tubing (Figure 11a). The heat-shrink tubing had an inner surface coated in heat-activated glue, which facilitated sealing, especially with the end caps.

The core was mounted vertically in the experiment in order to facilitate displacement of air, and so flow through the cement was from bottom to top. The lower PEEK endcap had separate inlets (for CO_2-rich fluid and for Ca-

rich water), and these were aligned with the cut in the cement core. The upper PEEK endcap had only a single outlet.

The core assembly was then sealed into a pressure vessel, which was placed into a fan oven (accurate to better than ±0.5 °C) and connected to inlet/outlet fluid conditioning/waste vessels and pumps, plus confining pressure line (Figure 11b).

a.

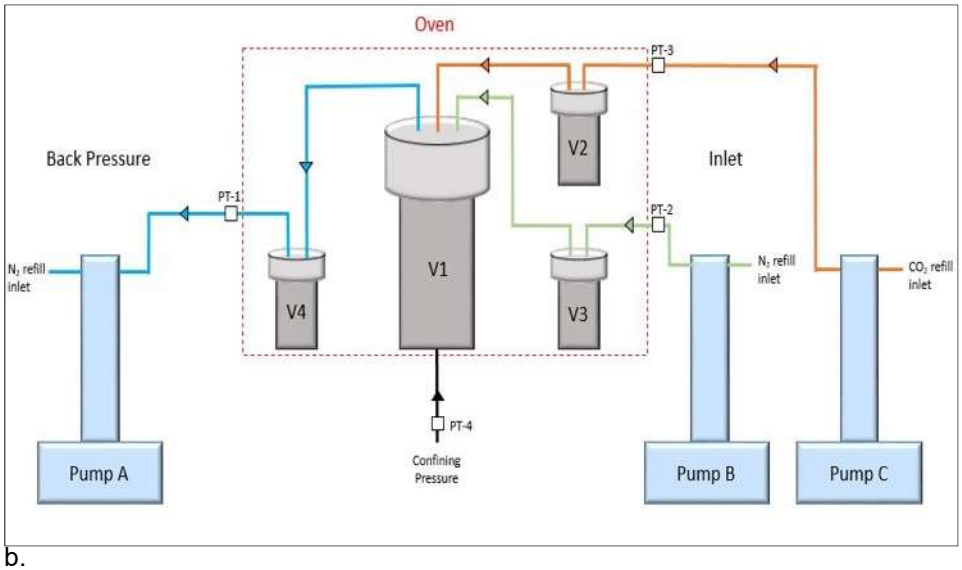

b.

Figure 11a. Photo of the set up within vessel 1 (V1). $Ca(OH)_2$ rich alkaline fluid and CO_2 inlets feed into the bottom of a cement core split in half and held together with heat shrink and PEEK end caps. A single outlet leads to a back pressure/waste vessel. b. Diagram of the experimental set up.

The orange, green, black and blue lines in Figure 1b are the CO_2 inlet, $Ca(OH)_2$ rich alkaline fluid inlet, confining pressure and back pressure respectively. V1, V2, V3 & V4 are the main reaction, CO_2 inlet, $Ca(OH)_2$ rich alkaline fluid and waste vessels respectively. In order to minimise equipment corrosion, the pumps were filled with gas, and the pressure of this transferred to solutions in the conditioning and waste vessels via gas/water interfaces. Pump A maintained a constant pressure to the flow line and withdrew fluid as necessary, Pump B supplied N_2 at a constant rate to flow the Ca-rich alkaline fluid, and Pump C supplied CO_2 at a constant rate. Note that for the experiment with free CO_2 there was no aqueous phase in vessel V2.

Run conditions were 50 °C and 100 bar, and with a confining pressure of 150 bar. The pressure differential ensured the PVC sheath tightly sealed onto the outer surface of the cement, and restricted flow to just the slice through it. A higher pressure differential was not used, in order to minimise the potential for the inner surface of the cement clamping together and restricting fluid flow.

Optimal ratios of dissolved Ca and CO_2 for carbonate mineral precipitation were calculated using PHREEQC V3 and the Pitzer database, and these served as a guide for the input flow rates in the experiments. The flow rates used were 0.99 ml/min $Ca(OH)_2$ solution, and 0.01 ml/min for both dissolved and free CO_2 (i.e. there was a higher mass of free CO_2 added compared to dissolved CO_2).

At the start of the experiments, some of the alkaline solution was flowed through the cement to allow measurement of average hydraulic permeability. Subsequent permeability measurements during reaction could then be compared to this. Note that as we did not have a measurement of the fracture aperture, the permeability values are calculated as an average across the entire 3.5 cm diameter cement core.

2.1.3 Analysis

Changes as a consequence of reaction were studied via mineralogical approaches only, as our primary interest was in the form and distribution of secondary precipitates (c.f. output fluid chemical composition which would be relatively constant once saturation was achieved, and we could not monitor it at high resolution in the areas

where precipitation was occurring). This was done by optical microscope, and also using Scanning Electron Microscopy (SEM), which provided high resolution. The SEM was run under variable pressure (VP) mode mode, as this meant that the sample did not have to be coated with a thin layer of either carbon or gold. In VP mode the electron beam ionises some of the low pressure gas in the SEM chamber, and the resulting shower of ions helps dissipate the electric charge that would otherwise build up on the sample. Whilst this is very useful for studying samples 'straight out of the reactor', it does resut in a slight loss of resolution.

2.1.4 Results

Three tests have been run at the time of writing this report:

1) Dissolved CO_2 reacting with alkaline fluid (Run 1862 interrupted by national lockdown and lab closures as a result of the Covid-19 pandemic).
2) Dissolved CO_2 reacting with alkaline fluid (Run 1863, a repeat of the above).
3) Free CO_2 reacting with alkaline fluid (Run 1864).

Planned experiments include:

4a) Long duration flow of just 0.55 M NaCl solution – to serve as control data (hopefully showing minimal impact of the experimental arrangement and thus confirming that changes we measure are related to chemical reaction between the two fluids).

4b) Either using the cement sample in 4a or a fresh piece of core if 4a shows too much reaction, flushing the sample with pure CO_2 (as a simulation of a leaking borehole), and then flushing the flow path with the Ca-rich alkaline fluid.

5) Use a solution of mixed alkalis (i.e. Ca hydroxide with NaOH and KOH) to see if higher pH will facilitate more precipitation of carbonate.

2.2 EXPERIMENTAL WORK ONGOING AT UNOTT

$MgCl_2$, $NaCO_3$, NaCl, HCl, and NaOH were of analytic reagent grade and used without further purification. Milli-Q water was applied to prepare aqueous solutions of 0.3 M $MgCl_2$ and 0.3 M Na_2CO_3. The experiments were conducted with 15 mL of simulated natural brines containing 0.3 M $MgCl_2$ and 0.3 M Na_2CO_3 in the control series, and the acidity, alkalinity, background electrolytes, and nanoparticle influenced experiments were conducted by adding HCl (10^{-5} M), NaOH (10^{-5} M), NaCl (0.5, 1.0, 1.5, 2.0 M), and Nano MgO particles (6, 12, 18, 24 mg), respectively (Table 4). All experiments were completed and duplicated. The reaction products were collected at 1, 2, 3, 4, 5, 6, 7 h using centrifuge tubes and cleaned two time with Milli-Q water. The liquids were then decanted after centrifugation for 5 minutes (4500 rpm). The residue solid was dried in an oven at 50 °C, and the weight of the reaction products was recorded.

Table 4. Summary of experiments

Variable	No.	HCl (mol/L)	NaOH (mol/L)	NaCl (mol/L)	Nano Mgo (mg)	$MgCl_2$ (mol/L)	Na_2CO_3 (mol/L)	Temperature (°C)
control	1	0	0	0	0	0.3	0.3	200
acidity	2	10^{-5}	0	0	0	0.3	0.3	200
alkalinity	3	0	10^{-5}	0	0	0.3	0.3	200
electrolytes	4	0	0	0.5	0	0.3	0.3	200
	5	0	0	1.0	0	0.3	0.3	200

	6	0	0	1.5	0	0.3	0.3	200
	7	0	0	2.0	0	0.3	0.3	200
nano Mgo (40-60 nm)	8	0	0	0	6	0.3	0.3	200
	9	0	0	0	12	0.3	0.3	200
	10	0	0	0	18	0.3	0.3	200
	11	0	0	0	24	0.3	0.3	200

The reaction products were analysed by X-ray diffraction (XRD) to identify the anhydrous magnesite. Bulk sample powders were scanned over a sampling range of 2 to 70 °2θ with a step size of 0.0131 and a scan speed of 0.082 °2θ per second, and a PANalytical X'Pert Pro was applied for these analyses by using Cu K-α radiation at 40 kV and 40 mA. Analysis of the peak intensities on the sample X-ray diffractograms enable evaluation (using DIFFRAC. EVA-XRD software) of the amount of different mineralogical components.

2.3 MINI-WELLBORE SIMULATOR SIMULATIONS

The ECCSEL Well Integrity[1] mini-wellbore simulator was used, and its results are simulated using MDEM. The MWS is presented in Figure 12. The system is composed of three hydraulic pumps: one for confining pressure, one for casing pressure and one for pore pressure (Figure 12a). These three pressures can be applied independently. The confining and casing pressures can be increased up to 20 MPa and 50 MPa, respectively. The main cell is composed of a thin core holder body in aluminium, wrapped with carbon fibre which is transparent to X-ray. Upper and bottom end caps, a confining sleeve and a steel casing complement the rig (Figure 12b). The casing of 40 mm outer diameter (and 37 mm inner diameter (ID)) is inserted into a rock formation with ID of 52 mm and outer diameter of 90 mm. The length of the sample is 290 mm. The 6 mm space between the casing and the formation is filled with the cement paste, which hardens to form the cement sheath (Figure 12c). The rock formation is put into a rubber sleeve onto which the confining pressure is applied. The MWS system can be used investigate different conditions affecting cement sheath, to apply a more realistic downhole stress condition. The casing pressure can be applied under constant confining pressure.

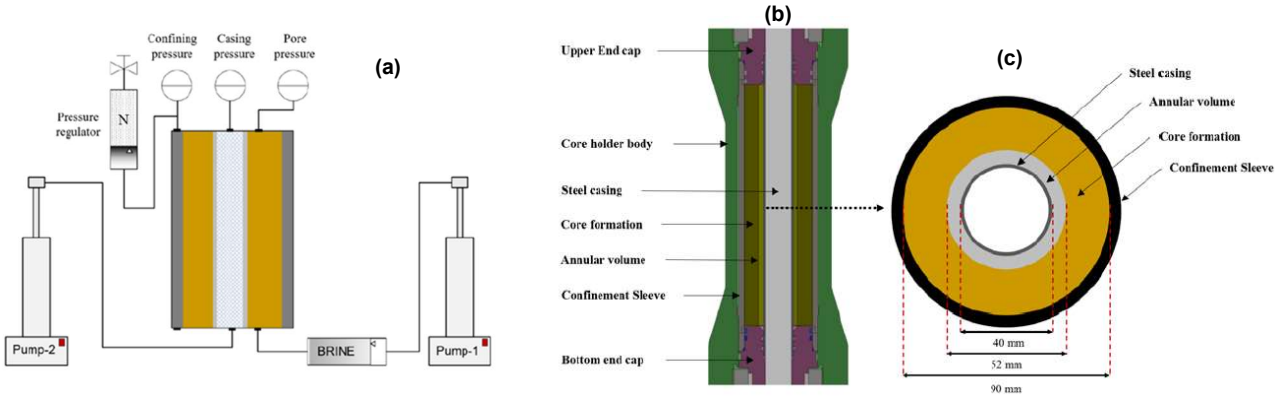

Figure 12. Mini-wellbore simulator (MWS)

Two tests were performed using this cell. The materials consisted of Castlegate sandstone, and a Portland G cement cured at ambient conditions of temperature and pressure or at 2 MPa for 48 hours. The first experiment was performed without a confining pressure, no pore pressure and the casing pressure increased to 45 MPa (Figure 13a). In the second experiment, the confining pressure was 8.5 MPa, the pore pressure in the rock and in the cement 5 MPa, and the casing pressure increased to 45 MPa (Figure 13b). Radial fractures are created as the casing pressure increases. Few radial fractures with higher sizes are obtained when there is no confining pressure.

[1] https://www.eccsel.org/facilities/storage/no310_sintef_wilab/

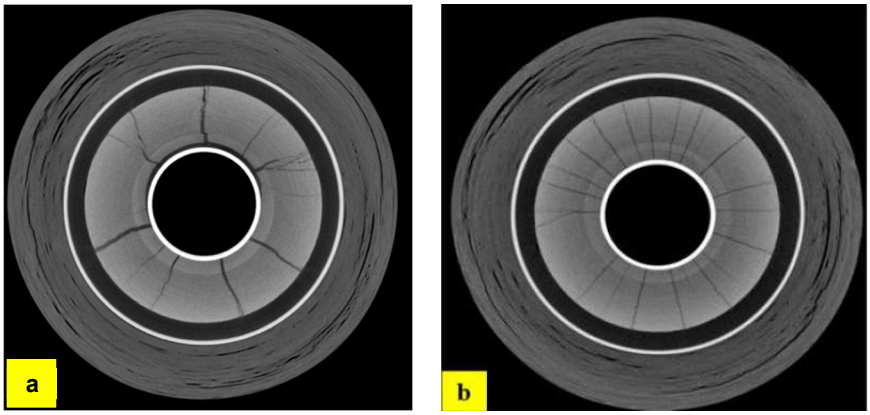

Figure 13. Radial fractures after a casing pressure increase.

3 Results

3.1 BGS REMEDIATION

Three tests have been run at the time of writing this report:

1) Dissolved CO_2 reacting with alkaline fluid (Run 1862, interrupted by national lockdown and lab closures as a result of the Covid-19 pandemic).
2) Dissolved CO_2 reacting with alkaline fluid (Run 1863, a repeat of the above).
3) Free CO_2 reacting with alkaline fluid (Run 1864).

The results of these are described below.

Planned experiments include:

4a) Long duration flow of just 0.55 M NaCl solution – to serve as control data (hopefully showing minimal impact of the experimental arrangement and thus confirming that changes we measure are related to chemical reaction between the two fluids).

4b) Either using the cement sample in 4a or a fresh piece of core if 4a shows too much reaction, flushing the sample with pure CO_2 (as a simulation of a leaking borehole), and then flushing the flow path with the Ca-rich alkaline fluid.

5) Use a solution of mixed alkalis (i.e. Ca hydroxide with NaOH and KOH) to see if higher pH will facilitate more precipitation of carbonate.

The results of these, plus further interpretation of 1-3 above, will be described in future WOP5 deliverables.

Experiment 1: Aqueous CO_2 case (Run 1862):

Vessel 2 (V2 in Figure 11b) was filled with 0.55 M NaCl (aq) and pressurized with 100 bar CO_2 at 50 °C. A magnetic stirrer bar was left running for 24 hours prior to initiating the experiment to ensure that the CO_2 had fully equilibrated with the solution.

The Covid-19 pandemic caused the emergency closure of the BGS laboratories and abandonment of this test after the reaction phase had happened (the subsequent experiment repeated these measurements). Though the loss of data maked interpretation of pemeability changes problematic, the reacted cement sample was still suitable for detailed mineralogical observation by SEM. The following are preliminary observations of the reacted cut surface of one half of the cement sample (Figure 14). Further study of this sample is ongoing, and some of these preliminary observations may be refined as new data are obtained.

Preliminary VP SEM work undertaken on the bottom (inlet) part of the left half of the core

Figure 14. Reacted cement core split open along the cut surface, and showing light-coloured precipitates.

VP SEM imaging reveals patches of different precipitates scattered across the surface of the cement (preliminary observations in Figure 15). A wide range of morphologies was observed: cubes and scalenohedral crystals, platelets and fibres, hexagonal, rosettes, and skeletal cubes. There is no immediately-obvious pattern to their distribution, which hints at either complex flow patterns, changing flow patters, far from equilibrium precipitation, or a combination of these (and other) processes.

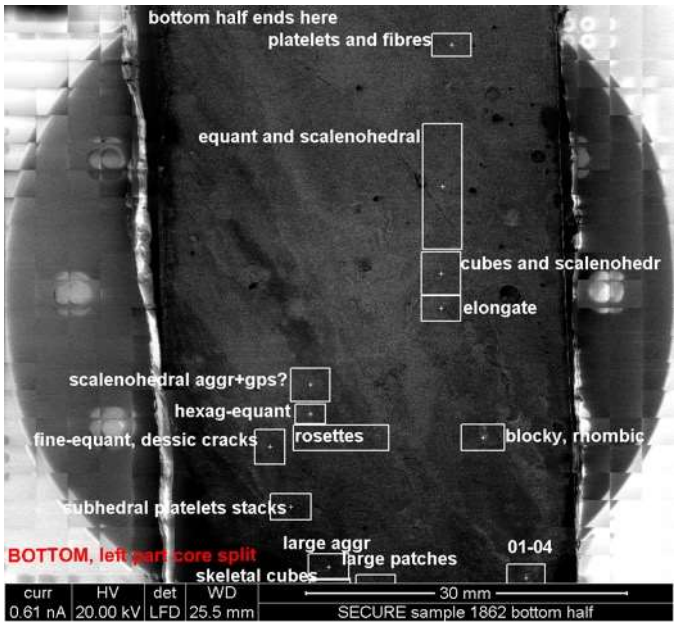

Figure 15. Low resolution SEM image of part of the reacted cement surface showing the distribution of a range of secondary phase morphologies (preliminary observations).

At the very base (immediate inlet end) of the core (Figure 16) the following were observed:

- Irregular patches of Ca rich phase with elongate crystals, possibly dendritic-like in places

- Skeletal crystals of Ca carbonate (likely but not definite at this stage)
- An anhedral mass of mixed composition

The first two of these are consistent with large degrees of supersaturation, and fast precipitation.

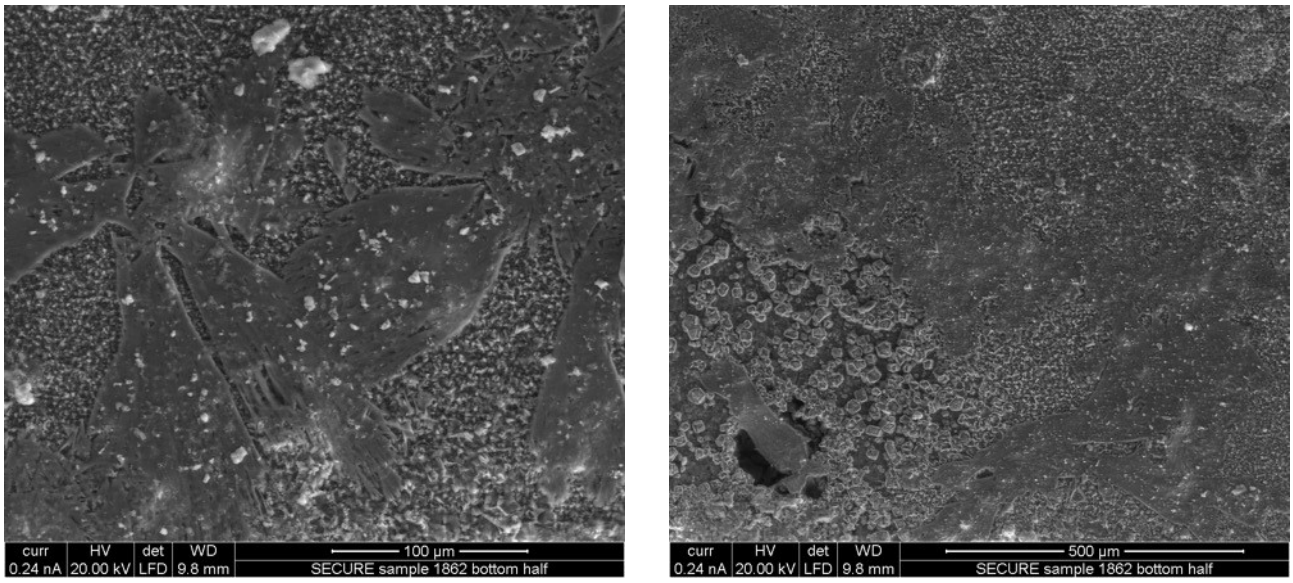

Figure 16a,b. Morphologies of precipitates at the very base (immediate inlet end) of the cement sample.

Higher resolution imaging of the lower part of Figure 16b shows rhombs and cuboids of carbonate precipitate (Figure 17a) that have likely undergone dissolution (spikey surface features) below a shell of later overgrowth (Figure 17b). It is currently unclear how these features formed, though possibilities include: repeated swings in fluid composition from saturated to undersaturated (and vice versa); and differential growth rates between edges and faces of crystals. Constraining which of these, or other, processes was involved will be a focus of future observations.

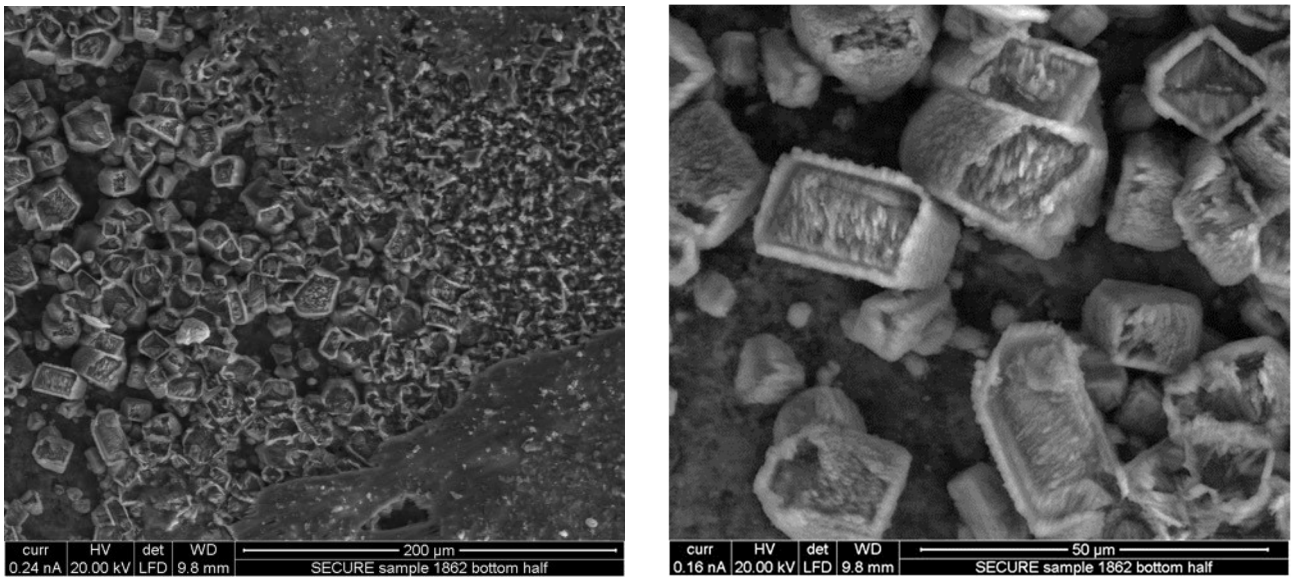

Figure 17 a,b. Close-up of the morphology of precipitates at the very base (immediate inlet end) of the cement sample.

A range of other morphologies of secondary phases covering the lower half (inlet end) of the cement sample were also observed. These include:

- Rhombs and scalenohedral aggregates (likely to be $CaCO_3$) (Figure 18a,b)
- A range of other morphologies that also appear to be $CaCO_3$ (Figure 19a,b)
- Masses of sub-micron phases of yet unresolved composition (Figure 20)
- Individual and intergrown scalenohedral crystals in finely crystalline mass (Figure 21)
- Highly fibrous precipitates. The composition of these was hard to establish using VP mode, but potential phases include gypsum/anhydrite and calcium silicate hydrate (CSH) phases (Figure 22a,b)

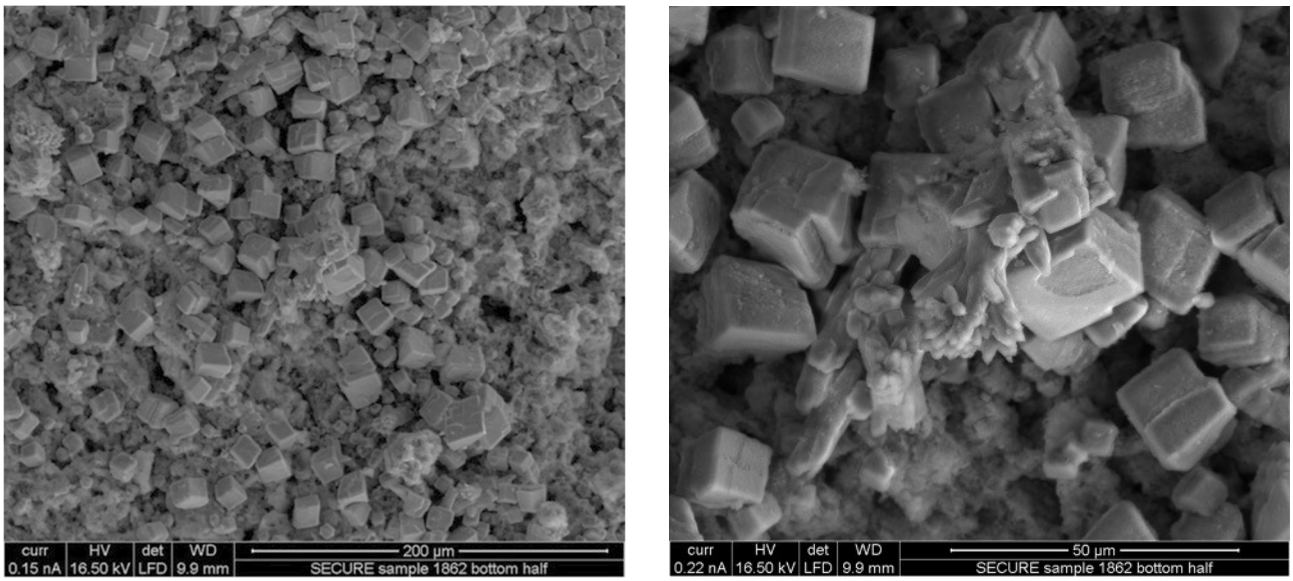

Figure 18a,b. Rhombs/distorted cubes and scalenohedral aggregates (likely $CaCO_3$).

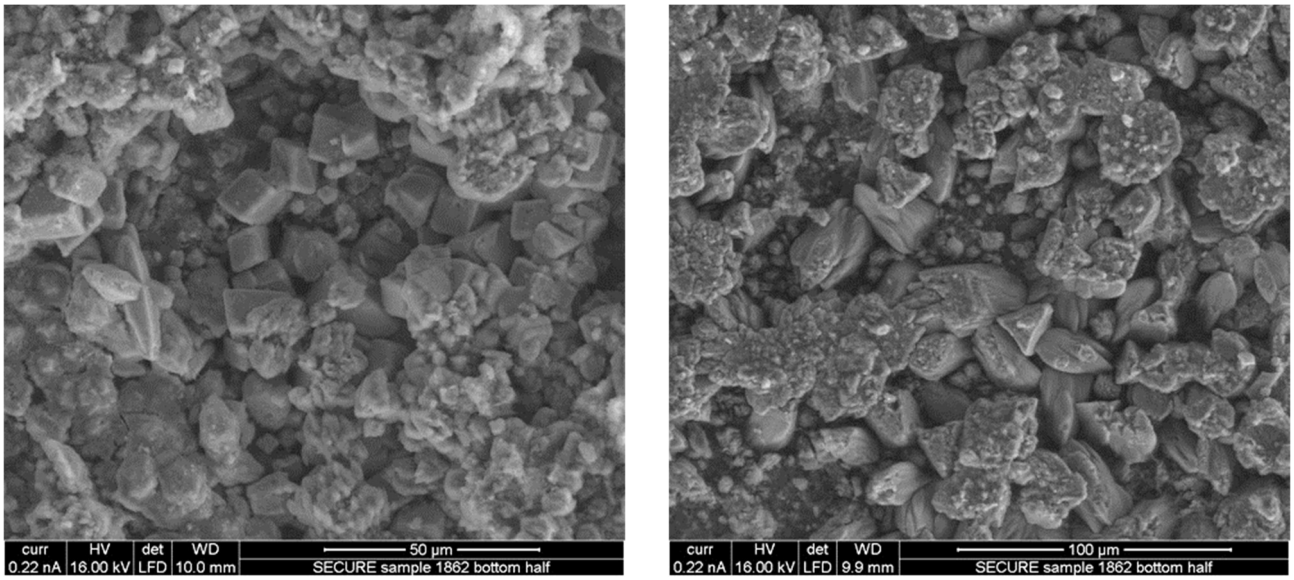

Figure 19a,b. Range of other morphologies of what appears to be $CaCO_3$ precipitates.

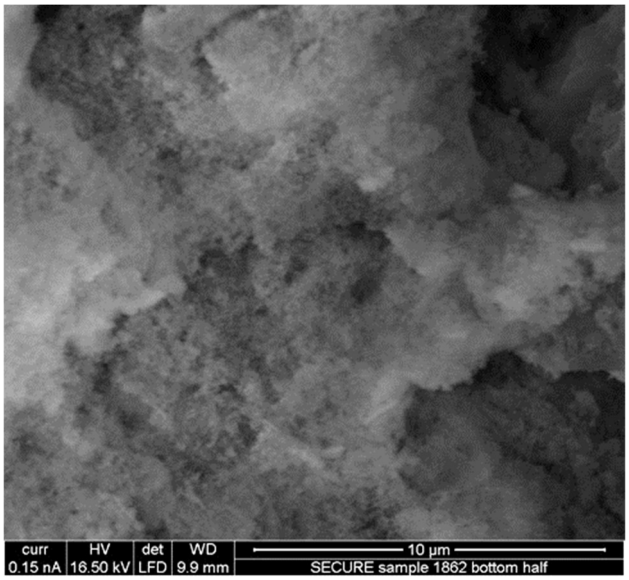

Figure 20. Highly porous masses of sub-micron phases (composition unresolved at the time of writing).

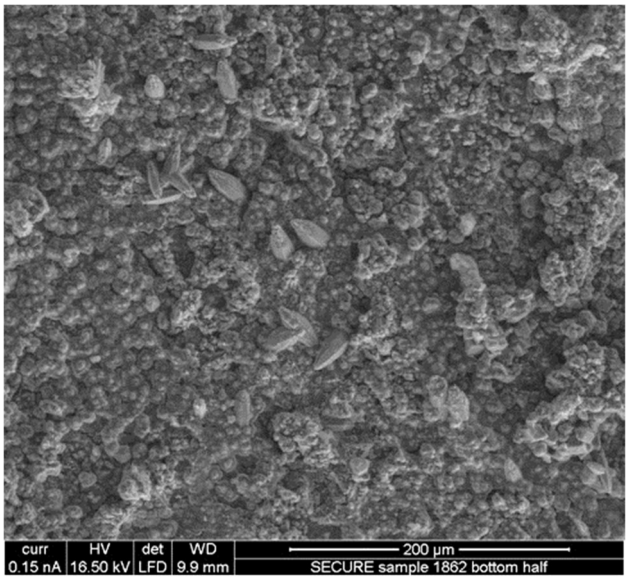

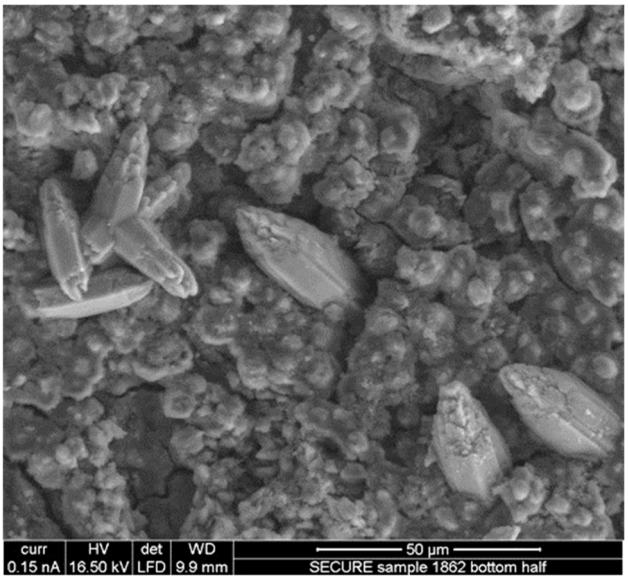

Figure 21a,b. Individual and intergrown scalenohedral crystals in finely crystalline mass. Note the cracks in places in (b), which might relate to sample desiccation (preliminary observation).

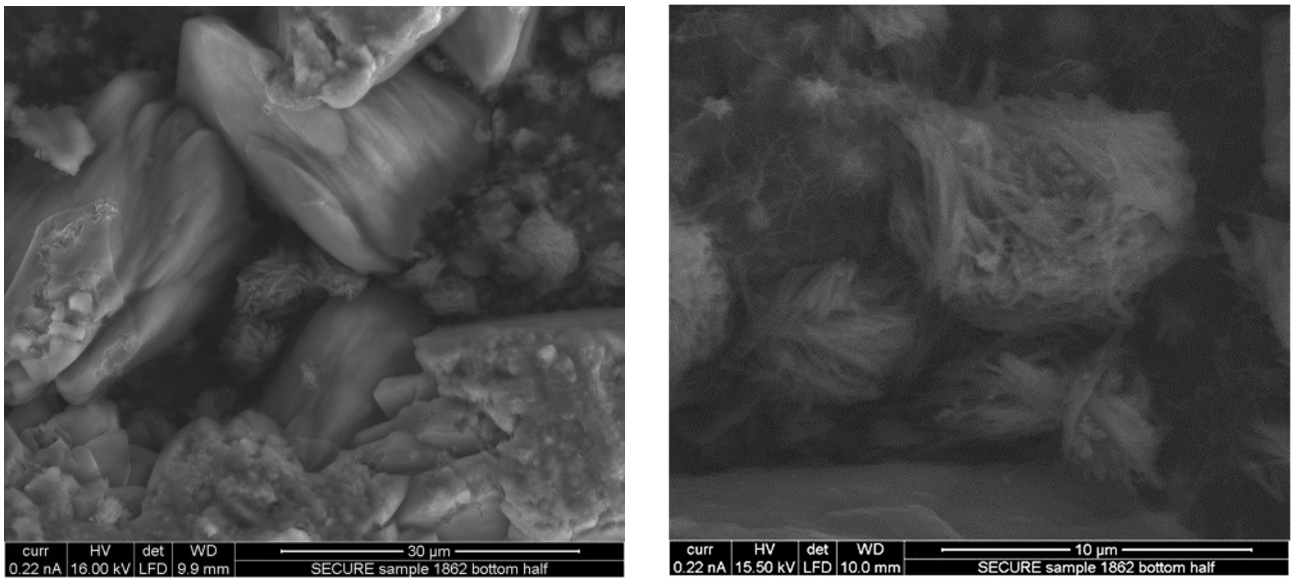

Figure 22a,b. Highly fibrous precipitates (composition uncertain at the time of writing, but these may include gypsum/anhydrite and CSH).

Work remains to be done to better characterise the complex nature of the precipitates and their origin in this sample. However, observations so far are consistent with complex mixing patterns of the CO_2-rich fluid with the alkaline Ca-rich fluid causing high degrees of supersaturation and rapid precipitation of a range of morphologies of $CaCO_3$. Most of the precipitates appear to have been derived from the injected fluids. However, if the composition of some of the fibrous phases (possible gypsum/anhydrite and CSH) is confirmed, then that would suggest that elements such as Si and S are being leached from the cement and the reprecipitated in the permeable zone.

Experiment 2: Aqueous CO_2 case (Run 1863):

This run was a repeat of the one above, though without the cessation in flow measurements caused by lab closures due to Covid-19. Vessel 2 (V2 in Figure 11b) was filled with 0.55 M NaCl (aq) and pressurized with 100 bar CO_2 at 50 °C. A magnetic stirrer bar was left running for 24 hours prior to initiating the experiment to ensure that the CO_2 had fully equilibrated with the solution. Figure 23a,b shows pressure and hydraulic permeability changes during initial, pre-reaction characterisation of the cement. Once the sample had stabilised, the average initial permeability was found to be 3.194 mD.

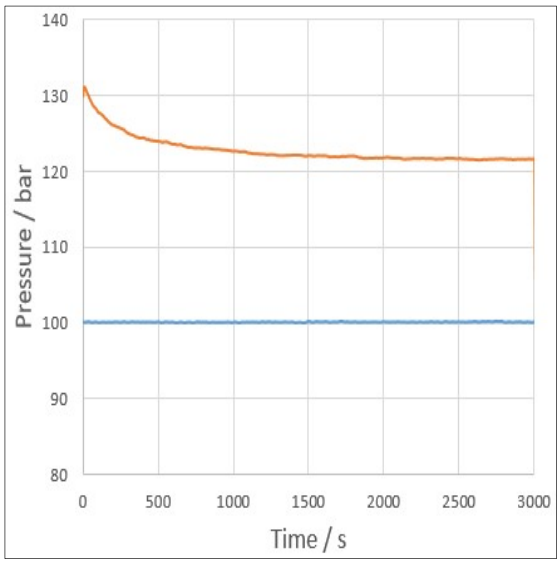

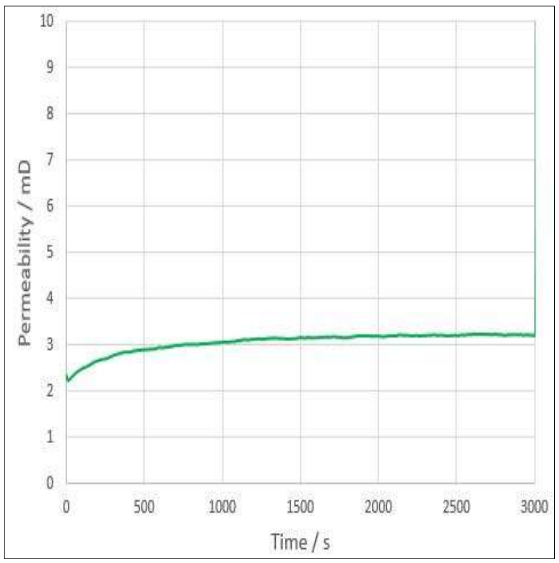

Figure 23a. Pressure changes during initial (i.e. pre-reaction) characterisation of the core, note inlet (orange) and outlet (blue) lines. b. Resultant permeability evolution towards a stable value.

Reaction of the saturated $Ca(OH)_2$ solution and dissolved CO_2 inside the cement caused an immediate and continued increase in system pressure (Figure 24) – presumably as a consequence of flow path blocking. Flow was stopped once system pressure reached 135 bar, in order to prevent exceeding the confining pressure. That inlet pressure decreased and outlet pressure increased after this showed that there was some continued connection across the core at first. However, the pressure differential stabilised, and a 20 bar pressure differential remained some 15 hours after the pumps were switched off. As well as suggesting that the blockage to flow remained in place, this also suggests that it may have 'matured' into something more impermeable than when initially formed.

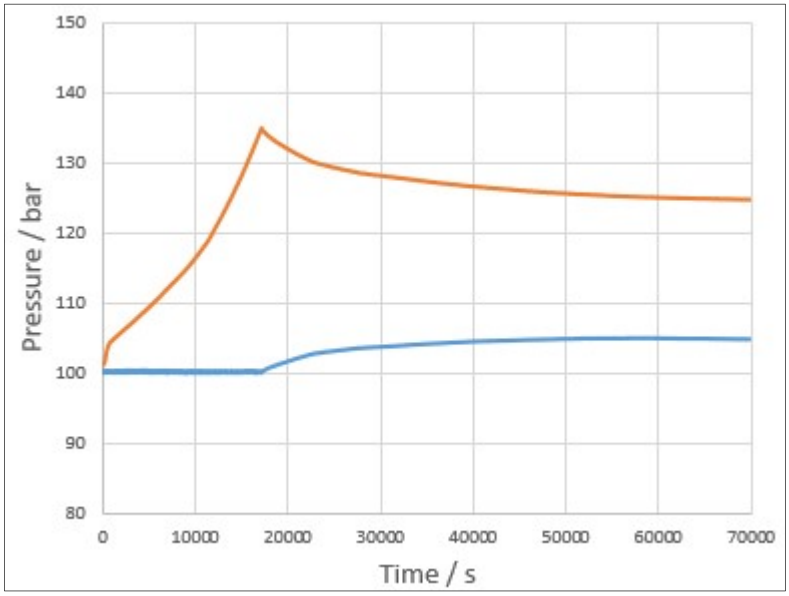

Figure 24. Relative pressure changes of the inlet (orange) and the outlet (blue) lines as the two reactant fluids are flowed through the cement core.

Pressure and flow data were used to calculate a plot of changing permeability during the initial phase (c. 17000 seconds) of the experiment (Figure 25). This shows permeability decreasing to 1.969 mD, at which point the pumps were turned off. Permeability would likely have decreased further upon continued reaction, but this would have required changing system parameters and running the experiment under constant differential pressure and monitoring flow changes – which we were not set up to do at the time.

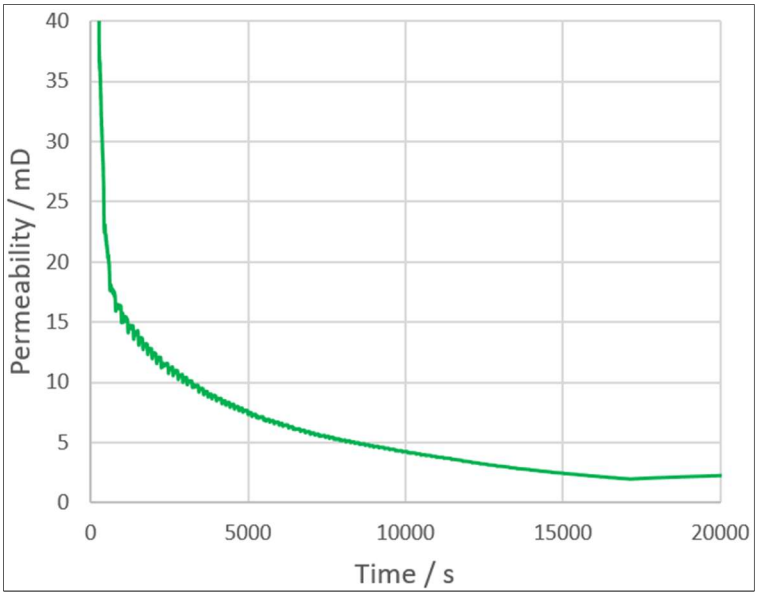

Figure 25. Average permeability during the reaction of $Ca(OH)_2$-saturated solution with dissolved CO_2 (note different timescale to Figure 3, with only the initial 20000 sec shown here).

Free CO_2 case (Run 1864):

This was a very similar experiment to that described above, but an extended pre-reaction characterisation of the sample was undertaken (50k sec as compared to 3k sec). Initial hydraulic permeability of the core was tested using alkaline fluid, and this stabilised relatively rapidly. A stable pressure differential was readily attained (Figure 26a), and a pre-reaction average permeability for the 3.5 cm diameter core of 0.444 mD was derived (Figure 26b). This value differs from the that obtained in the experiment described above. There could be several reasons for this difference, but the overall control factor was that each piece of sliced core was unique, and had slightly different aperture and fracture roughness.

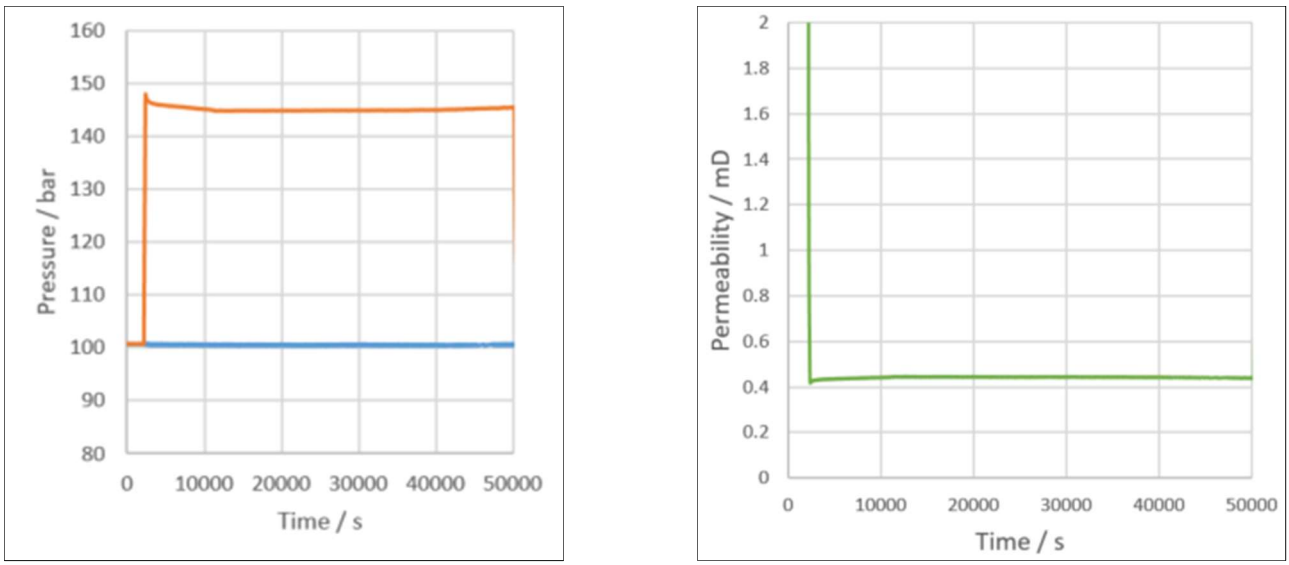

Figure 26a. Pre-experiment permeability test of the cement core shows relatively uniform differential pressure across the core. Permeability was derived from known flow rates and measured pressures at the inlet transducer (orange) and the back pressure (blue). b. Change and subsequent levelling out at 0.444 mD of permeability over the course of the pre-experiment permeability test.

The Ca-rich alkaline solution and free CO_2 (gas) were flowed through the core at 0.99 mL/min and 0.01 mL/min respectively. Inlet pressure increased (and hence so did differential pressure across the length of the core) as reaction caused precipitation and blocking of flow paths. This raised inlet pressure to a peak of approximately 147 bar in 5 hours 43 minutes, at which point flow was stopped in order to prevent exceeding the 150 bar confining pressure (continuing would have risked debonding and/or rupturing the PVC sheath). With flow stopped, pressure decay was monitored as small quantities of fluid migrated through the partly-sealed cement. This process was repeated twice more, both times showing rapid pressure increases as the fluids reacted and solids precipitated.

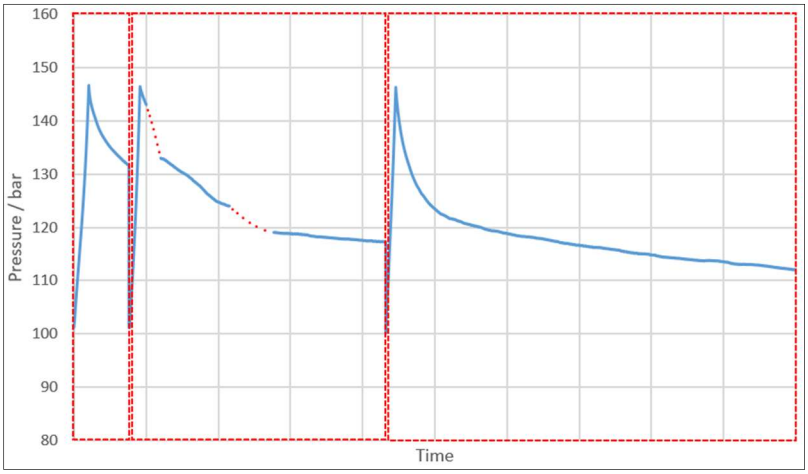

Figure 27. Combination of the inlet pressure changes as the free CO_2 experiment is cycled 3 times with sharper rises to ~148 bar. Each red box contains one cycle and the trail off of pressure afterwards. The red dotted lines indicate a break in recording due to site power-down. The sharp pressure increases took place in <6 hours each.

Pressure and flow data were used to derive average permeability for the 3.5 cm diameter core, and details of this for the injection periods (i.e. where pressure increased sharply in Figure 27) are shown in Figure 28.

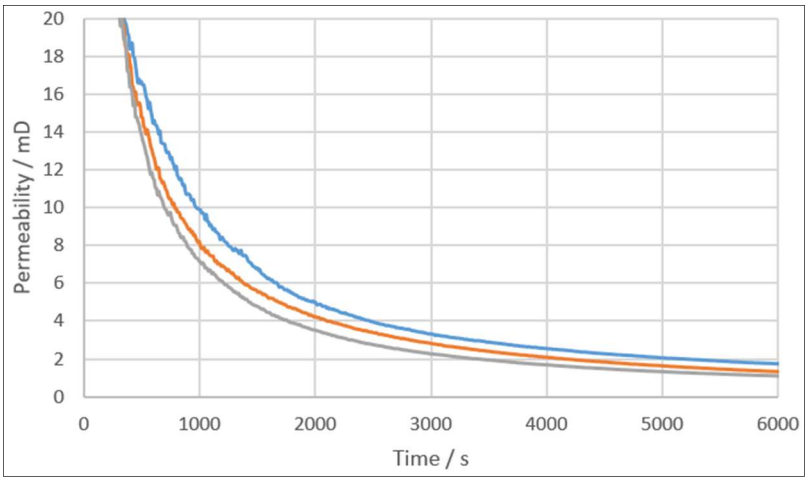

Figure 28. Average permeability during the reaction of $Ca(OH)_2$-saturated solution with dissolved CO_2. The blue, orange and grey lines represent the 1st, 2nd and 3rd cycles respectively showing a more rapid drop in permeability per cycle.

The progression to a more rapid decrease in permeability each time the test was run, suggests that precipitation has a larger impact on over time. Whilst we do not yet have mineralogical observations to help explain the processes involved (still to be undertaken at the time of writing), possibilities that are consistent include: a narrowing of flow paths with each phase of precipitation; a reduction in the number of flow paths; an increase in the number of $CaCO_3$ nucleation sites (i.e. 'seed crystals') over time, reducing delays in $CaCO_3$ growth linked to nucleation kinetics.

The average permeability of the 3.5cm diameter core was subsequently measured and found to have dropped to 0.413 mD (7% decrease).

3.2 MDEM SIMULATION OF NEAR-WELL FRACTURES

The experimental results are simulated using the MDEM code. The mesh for the different domains is shown in Figure 29. The x- and y-axes are the sizes of the domain in 2D and are given in meter. It consists of hole, casing, cement, interface between the casing and cement, the rock, the confining and outer regions. It can be observed that at the crossing of domains, the element sizes are affected, which could impact both the convergence time and the fracture patterns. A solution could be to reduce and keep a constant element size in all domains. It will improve the mesh, but significantly increase the number of nodes and thus, the computing power. A good compromise was found by adapting the size of elements based on their domain size, and as a rule, to refine the mesh from the outer region down to the casing. The parameters used in the simulation are given in Table 5, where tensile failure is prevented in the casing, hole, confining and outer regions by assigning an extremely high tensile strength. To prevent fluid flow from borehole to cement or from confining region to rock, a very low permeability is assigned to the casing and confining domain. The permeability of the rock (Castlegate sandstone) was also reduced for that purpose. Another modification will be to introduce a domain between the rock and the confining region which will play the role of a sleeve (with very low permeability) as shown in Figure 12c. Stiffness and Poisson's ratio of the cement paste in the annular space was estimated based on modelling presented by Agofack et al. (2019, 2020). The Young's modulus of Castlegate sandstone is around 2 GPa from unconfined compressive strength (UCS) tests but can be as high as 13 GPa under high confining pressure (Agofack et al., 2018).

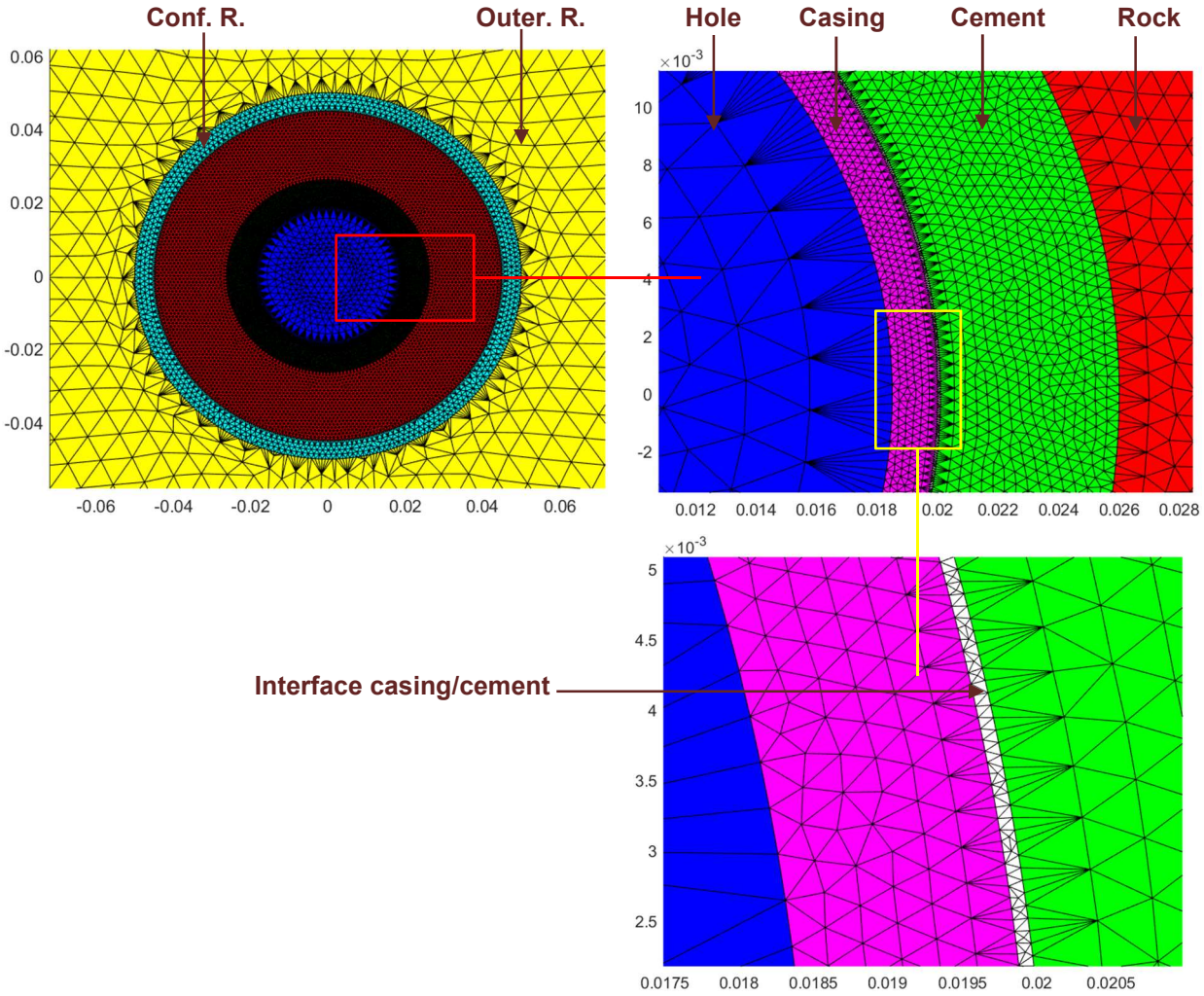

Figure 29. Mesh of different domains

Table 5. Domain parameters used in the simulation

material	Hole	Casing	interface	Cement	Formation	Conf. R.	Outer R.
Size: OD (m)	0.037	0.040	0.0402	0.052	0.090	0.100	0.5 x 0.5
E (GPa)	0.28	200	2	8.0	7	0.28	200
v [-]	0.45	0.3	0.15	0.15	0.25	0.45	0.3
φ [-]	0.95	0.02	0.40	0.40	0.29	0.95	0.02
k [m^2]	1×10^{-5}	1×10^{-21}	1×10^{-16}	1×10^{-16}	1×10^{-16}	1×10^{-21}	1×10^{-21}
σ_t (MPa)	10^{20}	10^{20}	0.1	7	2	10^{20}	10^{20}
STD_var of σ_t	0	0	0.3	0.3	0.3	0	0

The analytical solution of Figure 2 was derived in the previous section. This is numerically simulated, and its results are presented in Figure 30 for different hole pressures. The first fracture appears when the hole pressure is 10.5 MPa, higher than the outer applied (or confining) pressure. With further hole pressure increase, three created fractures are propagated from inner to outer surface of the rock, as suggested by the analytical solution.

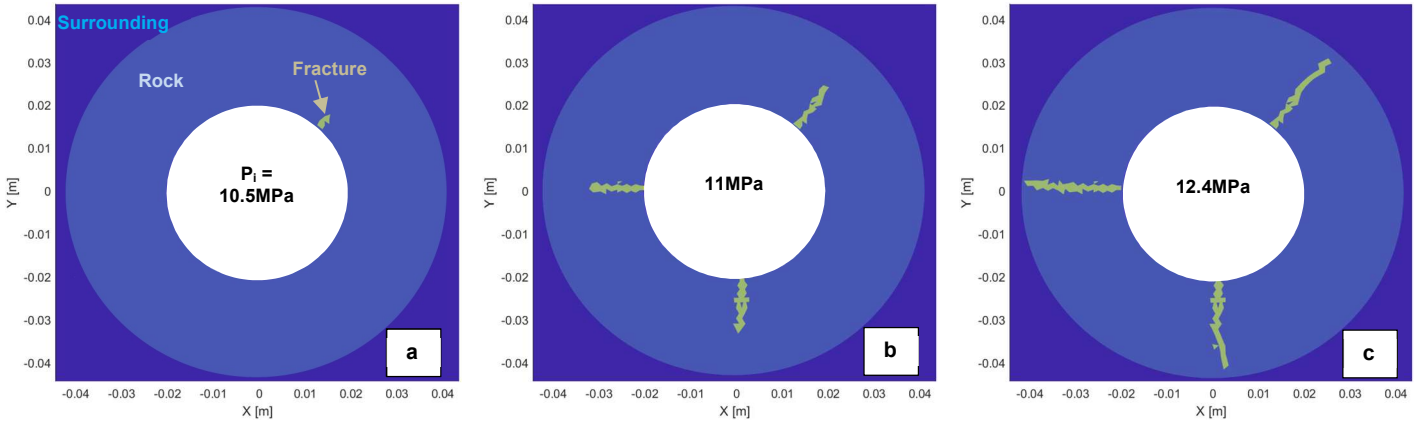

Figure 30. Effect of hole pressure on fracture propagation around the borehole, under a confining pressure of 7.5 MPa. No casing and no cement, and the rock properties are given in Table 5.

The results of the simulation are given in Figure 31 for different confining pressures and at different casing pressures. The left figures (a, d and g) are for a confining pressure of 7.5 MPa, while the middle and the right figures are for a confining pressure of 10 and 15 MPa, respectively. The figures in the first row (a, b and c) correspond to a casing pressure of 30 MPa, while the figures in the middle and bottom rows correspond to a casing pressure of 35 and 45 MPa, respectively. At a given confining pressure, the simulation results show that fractured elements and fracture propagation increase with the confining pressure. For example, at 10 MPa of confining pressure, the fractures are almost limited to the cement sheath area only, for casing pressure up to 35 MPa (Figure 31b,e), while at 45 MPa, some fractures propagated to the rock formation (Figure 31h). The confining pressure also strongly affects the fracture initiation and propagation. For example at a given casing pressure of 45 MPa, some fractures have propagated through the entire cement and rock system under a confining pressure of 7.5 MPa (Figure 31g), while there are only few fractures and limited to the cement sheath area under a confining pressure of 15 MPa (Figure 31i). In addition, under a confining pressure of 15 MPa, no fracture is created for casing pressure up to 35 MPa (Figure 31c,f). The results of Figure 31g are close to the experimental results presented in Figure 13, even though there is 1 MPa difference in confining pressure.

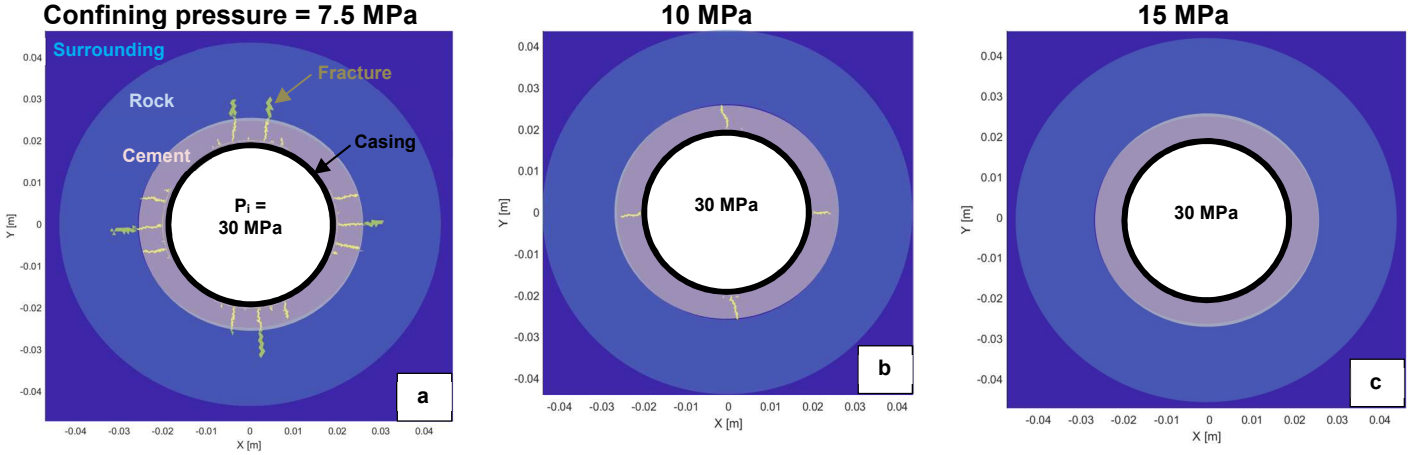

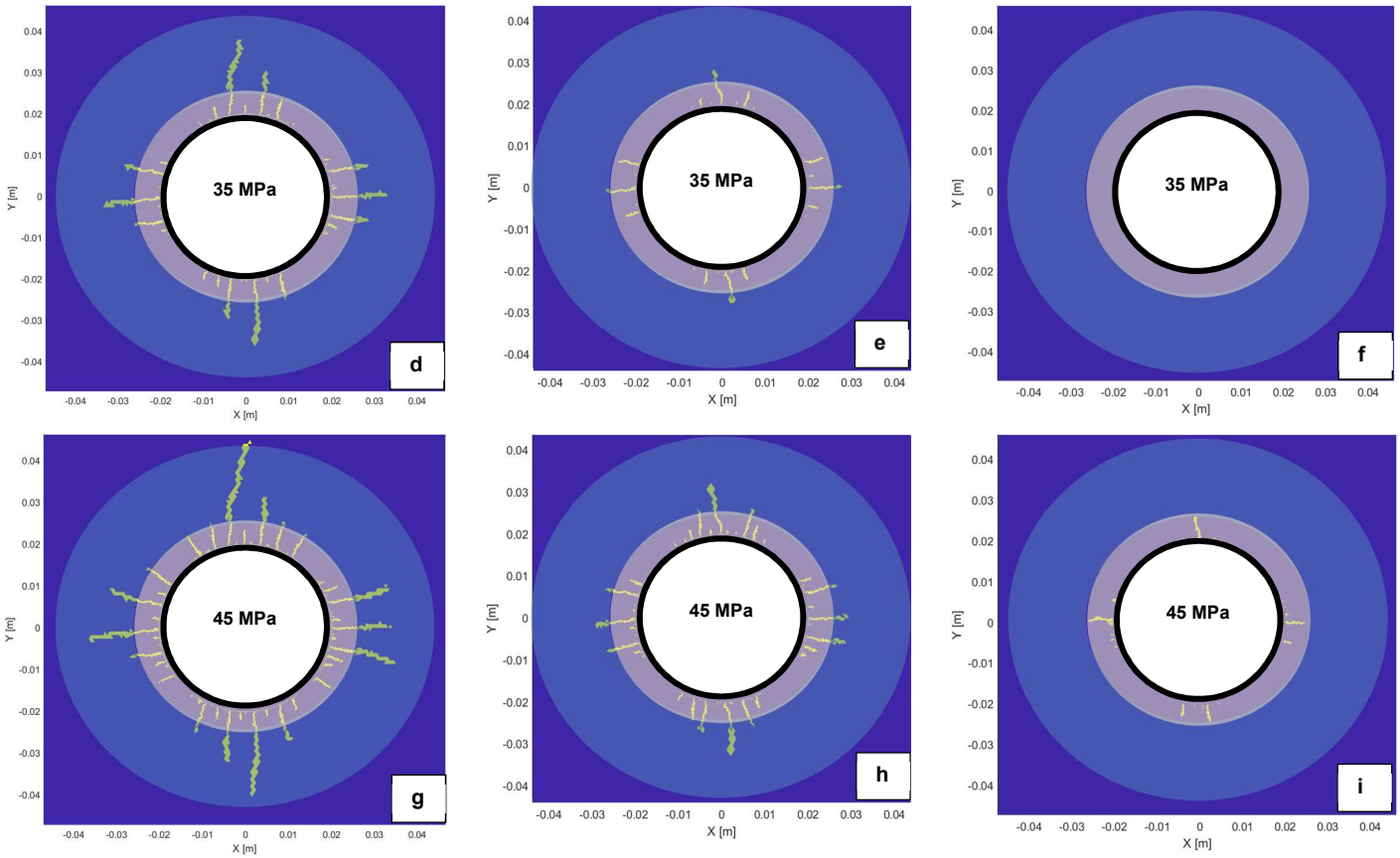

Figure 31. Effect of confining and casing pressures on fractures around the well

4 Discussion

The work reported here focused on laboratory testing of systems capable of precipitating solids into fractures occurring in the cement and rock surrounding a well. Testing is still at the small scale start phase, where focus is put on individual fractures, such that satisfying control can be exerted on the system and precise measurement of the permeability reduction caused by the precipitate can be obtained. The next step in testing should involve an intermediary scale and radial geometry particular to subsurface wells, as currently offered in the ECCSEL mini-wellbore simulator. From there, further upscaling may be done preferentially via numerical simulations, once the efficiency of the precipitated material in blocking several fractures can be experimentally established. A first step in that direction is to back analyse the stresses leading to the creation of fractures similar to those observed in the laboratory. Once reasonable agreement is obtained between simulations and experiments, the domains and boundary conditions may more easily be modified in order to explore fracture patterns with typical well dimensions embedded in large scale rock formations.

The aims of the experimental work were to demonstrate that controlled carbonate precipitation could lead to permeability reduction (and ideally sealing) of 'imperfect' borehole cement / drilling-induced damage in rock in the near-borehole region. A key aspect of this is that one half of the reaction involved was the migrating CO_2 (i.e. less 'remediating material' need be injected). This has been demonstrated, although no complete sealing of the cement could be obtained, since unlikely on laboratory timescales. However, flow paths got sealed enough for injection pressure to approach confining pressure. A secondary aim was to quantify the changes in permeability, and these were derived from the tests. However, permeability is given in terms of an average value for the 3.5 cm diameter sample used. As we do not accurately know the aperture of the slit through the sample, it is not possible to make an accurate assessment of permeability change specifically related to that. Also, each cut sample is 'unique', and it is difficult to make tight comparisons between samples.

A flow rig was constructed at BGS to allow controlled mixing of a CO_2-rich fluid with an alkaline Ca-rich fluid inside a sawn sample of cement. We used a sawn sample as it was a more controlled way to do the experiment. However, compared to the tortuosity of a 'real' fracture, this created a more 'prefect' and shorter flow path – and hence one having higher permeability. The system was initially beset by leaks in the reaction system and unstable pressures, and this slowed progress initially. On top of this, the coronavirus pandemic led to national lockdown in the UK, the emergency closure of the BGS sites, and the loss of some experiments (which needed repeating). This delayed progress further, and so we have concentrated on demonstrating that the proposed approach works, rather than on long-term tests or multiple repeat experiments scoping the impact of minor differences. The reaction is fast, leading to rapid precipitation of mainly carbonate, but also other phases.

We do not have a measure of just how much precipitate formed. Whilst we can visualise the 2D distribution of precipitation, not knowing the thickness of the precipitate means that we cannot generate a volume estimation. However, we observe very fast reaction, with flow paths becoming significantly sealed in just a few hours. Most of the precipitation appears to be related to the Ca and CO_2 added to the flow zone via the fluids. However, there appears to be possible evidence for some leaching of elements from the cement (possibly Si and S), which are then reprecipitated in the flow zone. This is a tentative observation at the time of writing, and ongoing work will attempt to confirm this. Carbonate precipitates take the form of rhombs, many of which show complex features, and these rhombs coalesce into sheets that line and fill void space. Processes controlling the complex features may include dissolution the overgrowth, or fast growth of hopper skeletal crystals, and ongoing work will hopefully clarify this.

We do not yet know what all the phases are that we can see, in part because we do not have a detailed composition for them. However, a key observation is that many are not completely 'solid'. In other words, there are growths looking like rosettes of sheets, or loose masses of rhombs. The entrainment of space within these type of precipitates increases their effective molar volume – i.e. less mass of material needs to precipitate to achieve the same degree of permeability reduction. The rhombs of carbonate show a range of textures (e.g. possible dissolution & overgrowths, possible high degrees of supersaturation and the formation of hopper skeletal crystals). Whist we cannot completely rule out 'quenching' effects at the end of the experiments, such a range of features would be consistent with switching of fluid flow paths during precipitation plus different degrees of fluid mixing near the injection points – both could drive very localised variation in degree of saturation state (i.e. swing the solution from (super)saturated to undersaturated and back again, possibly several times).

The textures of secondary precipitates, and the range of them, are consistent with fast precipitation. This implies significant oversaturation and is something that would be expected from the mixing of reactive fluids. A consequence of this is that the precipitates are governed (at least in part) by precipitation kinetics rather than just thermodynamics, and that over time initially-formed phases may be replaced by more stable ones (e.g. amorphous / less ordered ones being replaced by more ordered ones, or clusters of many small rhombs being replaced by fewer, larger crystal). Given the relatively short duration of the lab experiments, we would not expect to see the end point of such 'maturation' of precipitates. However, there have been 'natural analogue' studies of calcium silicate hydrate (cement mineral) carbonation and also carbonation of hyperalkaline fluids which show that denser and more stable products will dominate over time (e.g. Rochelle and Milodowski, 2013).

Precipitation rapidly led to a reduction in flow paths, which for a constant flow rate led to an increase in differential pressure across the samples, and an overall decrease in permeability. At a laboratory-scale therefore, we have demonstrated that controlled carbonate precipitation can greatly reduce the permeability of imperfectly-sealing borehole cement. Additional experiments are underway to further characterise the rates of flow path sealing and the nature of the precipitates, and these will be reported in subsequent WP5 deliverables/publications.

Another path was pursued at UNOTT, allowing remediation of fractures further away from the well and thus not necessarily in the presence of cement. Here the research aims at precipitating magnesite to provide a more acid-resistant mitigation strategy. Current research continues to improve the precipitate properties, looking at high temperature reactions with added nanoparticles to further reduce the remediation material's porosity and provide increased blockage. The work described here can be seen as preliminary reporting, to be followed shortly in the later D5.8 deliverable early in 2021.

Once these remediation fluid compositions and preparation methods from both BGS and UNOTT will be optimised, further testing and improvement can be achieved by scaling up remediation tests using the ECCSEL mini-wellbore simulator. Being part of the international ECCSEL research infrastructure network, this setup is particularly well-suited to be used in such qualification experiments with planned visits and stay of scientists

at the SINTEF facility. Initial remediation testing has already been described in report deliverable D5.4, with low-density Portland cement, not requiring dual fluid flow (remediation fluid and CO_2 gas). Some modifications will be needed to test the BGS and UNOTT remediation fluids in the mini-wellbore simulator, principally coupling more pumps to co-deliver CO_2 and the remediation fluid and a means to deliver the fluids at desired temperature. These upgrades are deemed relatively easy to put in place and will be pursued in the coming months.

The second part of this report was dedicated to proposing a modelling approach in order to carry the laboratory investigations over to time- and cost-effective numerical investigation of different field scenarios in which the remediation strategies would be deployed. The first steps in this endeavour were chosen to consist of adapting a tool capable of recreating the fracturing observed in the mini-wellbore simulator (MWS); the rationale behind this choice was that the fact that the MWS already takes a first step towards field-realistic geometry and system components. The geometry is a concentric radial stacking of materials as is the case in real wells, albeit at a reduced scale to be still manageable inside a CT scanner. The modelling was thus based on the laboratory initial configuration, with as accurate as possible input of needed material properties. The in-house MDEM tool was chosen to perform the simulations as it has proven to be able to recreate much more realistic fractures than other tools, such as purely finite elements or discrete elements (these last do a better job if complex particle aggregates are used).

Some compromises were needed to obtain satisfactory and semi-quantitative match between the simulation results and the laboratory experiments detailed in report D5.4. These can be summarized by stating that the MDEM software was conceived for porous rocks and therefore it was not straightforward to include steel casing and rubber sleeve, without having rigorous interfaces between them and the geomaterials. Interface transitions are best captured with a detailed mesh, however computing time becomes excessive if the whole domain is discretized in great detail, especially as fracturing starts to develop. It is thus very tempting to reduce the modelling domain extent, although this is not easily done without compromising accurate representation of applied stresses, especially in the isotropic case. Eventually, it was possible to correctly calibrate the model to recreate the observed fracturing from the experiments. Once this is achieved, it is a straight-forward matter to upscale dimensions to field well sizes. At the same time, the restrictions on the outer boundary (such as impermeable cell wall and isotropic confining stress) can be lifted and the domain size increased. The next step would be to either transfer the fracture topology to a fluid dynamics simulator (this has already been performed for simpler cement debonding tests) to evaluate numerically the fracture network permeability or to continue simulations inside MDEM, but replacing the fractures with intact elements with corresponding properties to the remediation materials described in this report.

5 Conclusions

The first phase of experiments aimed at sealing flow paths in the borehole/near borehole region via controlled precipitation of $CaCO_3$, have shown that:

- Reaction is fast, leading to rapid precipitation of mainly carbonate, but also other phases.
- Carbonate precipitates take the form of rhombs, many of which show evidence of complex internal features, and these rhombs coalesce into sheets that line and fill void space.
- Precipitation rapidly led to a reduction in flow paths, which for a constant flow rate led to an increase in differential pressure across the samples, and an overall decrease in permeability.

At a laboratory-scale therefore, we have demonstrated that controlled carbonate precipitation can greatly reduce the permeability of imperfectly-sealing borehole cement.

Additional experiments are underway to further characterise the rates of flow path sealing and the nature of the precipitates, and these will be reported in subsequent WP5 deliverables.

The other remediation system has shown promising results when magnesite is precipitated with added nanoparticles or other additives to stabilise it. This route will continue to be investigated to create a stable precipitate, capable of handling acidic conditions in its interaction with leaking CO_2.

A numerical model stage was created and shown to quantitatively reproduce fracturing observed in the complex geometry of the mini-wellbore simulator. This model can be used to design new tests in the laboratory in an optimised way, by predicting conditions for creation of certain types of fractures and limit stress values to stay clear of integrity breach conditions. Moreover, the model lends itself to upscaling in both internal and outer boundary dimensions and conditions, which will be useful to analyse full scale field scenarios. The obtained fracture networks and their extensions away from the well will inform on possible remediation strategies and optimisation work needed for good placement of remediation fluids.

Glossary

API American Petroleum Institute.

BFS Blast furnace slag.

BWOC By weight of cement.

CT X-ray computed tomography.

O&G Oil and gas.

6 References

N. Agofack, Micromechanical and homogenization modelling for a hydrating oilwell cement paste, ARMA, New York, NY, USA, 2019.

N. Agofack, S. Ghabezloo, J. Sulem, Chemo-poro-elastoplastic modelling of an oilwell cement paste: Macroscopic shrinkage and stress-strain behaviour, Cement and Concrete Research 132 (2020).

N. Agofack, S. Lozovyi, A. Bauer, Effect of CO2 on P- and S-wave velocities at seismic and ultrasonic frequencies, Int J Greenh Gas Con 78 (2018) 388-399.

H.T. Alassi, Modeling reservoir geomechanics using discrete element method: Application to reservoir monitoring, Norwegian University of Science and Technology, 2008.

H.T. Alassi, R. Holt, Relating discrete element method parameters to rock properties using classical and micropolar elasticity theories, International Journal for Numerical and Analytical Methods in Geomechanics 36(10) (2012) 1350-1367.

S. Gheibi, S. Sangesland, T. Vrålstad, NUMERICAL MODELING OF RADIAL FRACTURING OF CEMENT SHEATH CAUSED BY PRESSURE TESTS, Proceedings of the ASME 2019 38th International Conference on Ocean, Offshore and Arctic Engineering OMAE2019, ASME, Glasgow, Scotland, 2019.J.C. Jaeger, N.G.W. Cook, R.W. Zimmerman, Fundementals of rocks mechanics, 2007.

C.A. Rochelle and A.E. Milodowski (2013). Carbonation of borehole seals: comparing evidence from short-term lab experiments and long-term natural analogues. Applied Geochemistry 30, 161–177, 10.1016/j.apgeochem.2012.09.007

M. Rongved, P. Cerasi, Simulation of Stress Hysteresis Effect on Permeability Increase Risk Along A Fault, Energies 12(18) (2019).